Volume 6 · Issue 1 · March 2023 | ISSN 2810-935X (Online)

BILINGUAL PUBLISHING GROUP
Pioneer of Global Academics Since 1984

Journal of Mechanical Materials and Mechanics Research

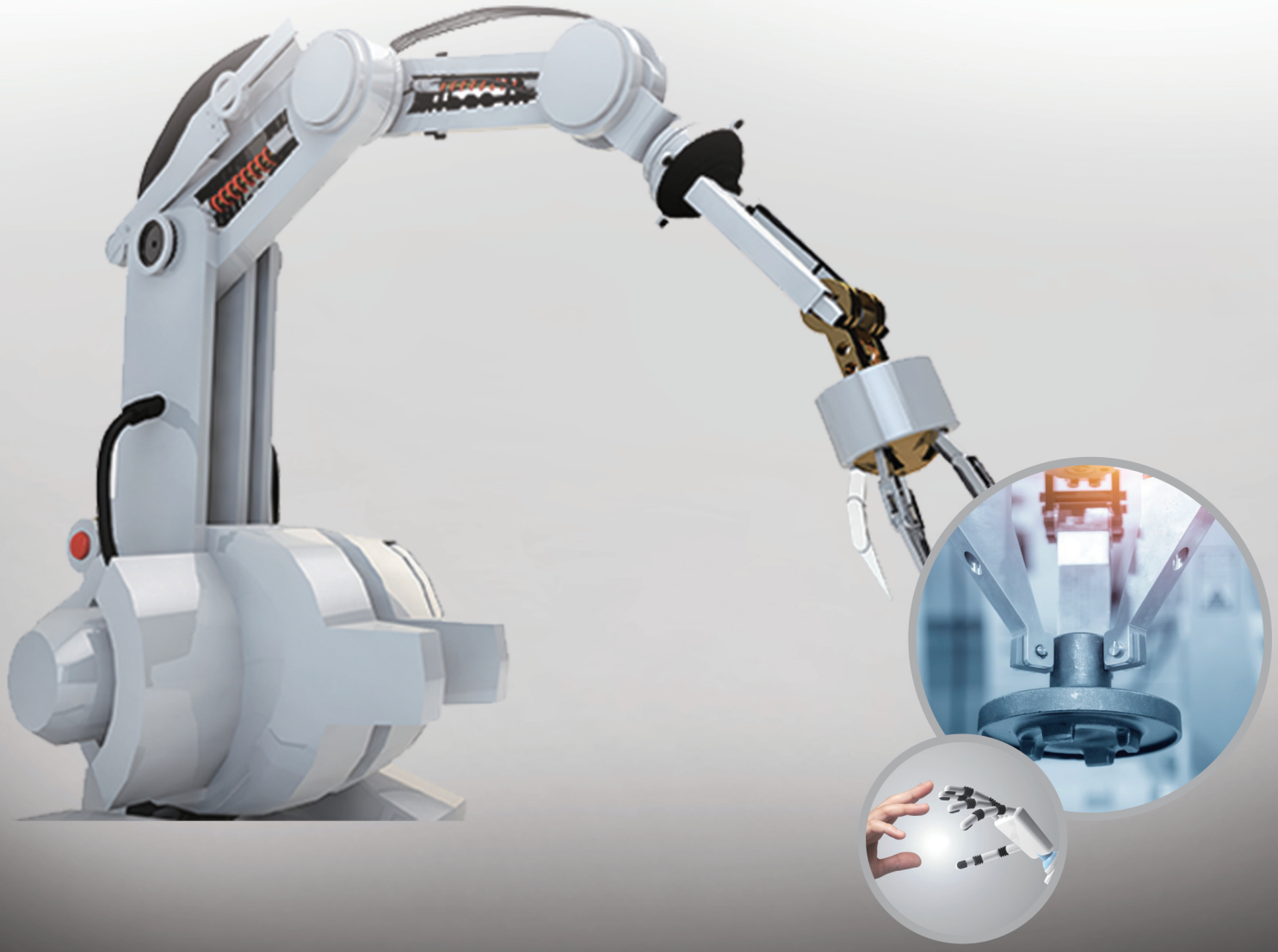

Volume 6 Issue 1 • March 2023 • ISSN 2810-935X (Online)

Journal of Mechanical Materials and Mechanics Research

BILINGUAL PUBLISHING GROUP

Pioneer of Global Academics Since 1984

BILINGUAL PUBLISHING GROUP
Pioneer of Global Academics Since 1984

Volume 6 | Issue 1 | March 2023 | Page1-53
Journal of Mechanical Materials and Mechanics Research

Contents

Articles

BILINGUAL PUBLISHING GROUP
Pioneer of Global Academics Since 1984

Journal of Mechanical Materials and Mechanics Research
https://journals.bilpubgroup.com/index.php/jmmmr

ARTICLE

Estimation and Analysis of Structural Responses of Asphalt Pavement Using Interlayer Contact Bonding Model

***Xuntao Wang*[1*], *Hu Wang*[2]**

[1] *Xi'an Shiyou University, Xi'an, Shaanxi, 710065, China*
[2] *Chang'an University, Xi'an, Shaanxi, 710064, China*

ABSTRACT

The interlayer contact condition of asphalt pavement has a significant impact on stress transfer and energy dissipation with adjacent layers, so a model considering the bonding condition of adjacent layers is introduced for evaluating the structural response of asphalt pavement. The pavement structure, the material characterization with temperature, the interlayer contact bonding model, the types of bond failure, and the prediction method of pavement life are described in detail. Results show that the transversely tensile strains at the top of asphalt pavement under the condition of high temperature were easy to cause the top-down cracking outside the edge of the dual tire. The bonding failure has a significant influence on strains at the bottom of the surface course with the condition of high temperature, especially, the longitudinally tensile strains would increase obviously as the disengaging area between the surface course of asphalt pavement and the base layer increases. Finally, it is proved that the surface course is vulnerable to form deformations and cause damage under the combined action of low speed and high temperature

Keywords: Asphalt pavement; Interlayer contact; Bonding condition; Structural response; Strain

1. Introduction

Asphalt pavement is widely used in pavement design and actual engineering due to the effectiveness of distributing and transferring the vehicle load to the subgrade layers. Up to now the evaluation model of the structural response of asphalt pavement is still a crucial part of pavement design and performance prediction. Asphalt pavement is routinely described as a multi-layer composite structure, and the structur-

*CORRESPONDING AUTHOR:
Xuntao Wang, Xi'an Shiyou University, Xi'an, Shaanxi, 710065, China; Email: wxt5288@126.com

ARTICLE INFO
Received: 26 November 2022 | Revised: 30 December 2022 | Accepted: 13 January 2023 | Published Online: 16 February 2023
DOI: https://doi.org/10.30564/jmmmr.v6i1.5288

CITATION
Wang, X.T., Wang, H., 2023. Estimation and Analysis of Structural Responses of Asphalt Pavement Using Interlayer Contact Bonding Model. Journal of Mechanical Materials and Mechanics Research. 6(1): 1-15. DOI: https://doi.org/10.30564/jmmmr.v6i1.5288

al responses of this system are significantly affected by the interlayer condition between adjacent layers [1]. A good interlayer condition between adjacent layers will increase the strength at the contact interface and make different layers of pavement form a monolithic structure to resist the action from the environment and traffic. In contrast, the shear strength between pavement layers will be reduced, and it will be easy to cause pavement distresses and shorten the service life of the asphalt pavement.

There are two common assumptions of interlayer condition between adjacent layers in some previous research [2-4], one is full-bond condition and the other is no-bond condition. However, this is an impractical assumption and an extreme condition to the real pavement structure. BISAR software was usually used to simulate the pavement structure and compute the response of asphalt pavement [5,6]. The model in BISAR generally uses some possible values of the sliding coefficient to simulate the interface condition. Nevertheless, it is difficult to obtain the real value of the sliding coefficient and can't simulate the actual interlayer contact condition of adjacent layers. Some researchers [1,7,8] held the interlayer condition of pavement structure lies in someplace between the bonded condition and the unbonded condition. In this research, the contact element and target element are applied to simulate the function of bonding material between adjacent layers, and this is different from the finite element calculation of previous studies. Otherwise, the model used in this paper is the interlayer contact bonding model, and it will be explained and illustrated in the following text.

Previous research has shown that the interlayer bonding condition plays an important role in accurately calculating and predicting the responses of asphalt pavement [9-11]. So this paper will investigate the structural responses of asphalt pavement with the interlayer contact bonding model and analyze the pavement performance. The Modified Havriliak—Negami model is utilized to describe material characteristics of asphalt mixtures at different frequencies and temperatures, and construct the dynamic modulus master curve of asphalt mixtures according to the datum from the citation. The detailed calculations for the structural responses of the typical asphalt pavement were executed under vehicle load and different temperatures.

2. Methodology

2.1 Pavement structure and vehicle loading

The road structure is comprised of four different layers from top to bottom [12], which includes the asphalt concrete layer, semi-rigid base, subbase, and subgrade. Meanwhile, the asphalt concrete layer (the surface course) is divided into three sublayers, the upper layer (ACUL for short), middle layer (ACML for short) and lower layer (ACLL for short). The pavement structure is shown in **Figure 1**, which is symmetric along the Y axis. For the purpose of minimizing the effect of boundary condition and mesh size on finite element calculation in ANSYS, the final structure size of asphalt pavement is 305 cm in width and 720 cm in length, and this is gotten by a large number of numerical tests and previous experiences. The structural responses at different locations of asphalt pavement are monitored by using the three points shown in **Figure 1**, and these responses are the displacement of point A, which locates at the surface of ACUL along the Y direction (U_{YA} for short), the strains of point B, which locates at the bottom of ACLL along the X direction and the Z direction (ε_{XB} and ε_{ZB} for short), and the strain of point C, which locates at the top of subgrade along the Y direction (ε_{YC} for short), respectively. In this study, these responses will be applied to predict the behaviors of asphalt pavement and analyse the performance of the pavement structure [13,14].

The mesh size near the loading area is relatively fine, and the meshing is 5 cm along X direction and 4.5 cm along Z direction, respectively. The mesh size in other areas is relatively coarser, and the meshing is 10 cm along X direction and 9 cm along Z direction, respectively. The finite element model of the pavement structure is shown in **Figure 2**. There is a vehicle load with a single tire, which is applied on the surface of ACUL, and the tire load is 0.7 MPa. It

is assumed that the loading footprint is a rectangle, which is 20 cm long and 18 cm wide [15-17]. In addition, considering the action of rolling friction between the tire and ACUL in the horizontal, the force of rolling friction f between them is determined by Equation (1):

$$f = \mu P \tag{1}$$

in which μ is the coefficient of rolling friction, and it equals 0.012 in this study. P represents pressure.

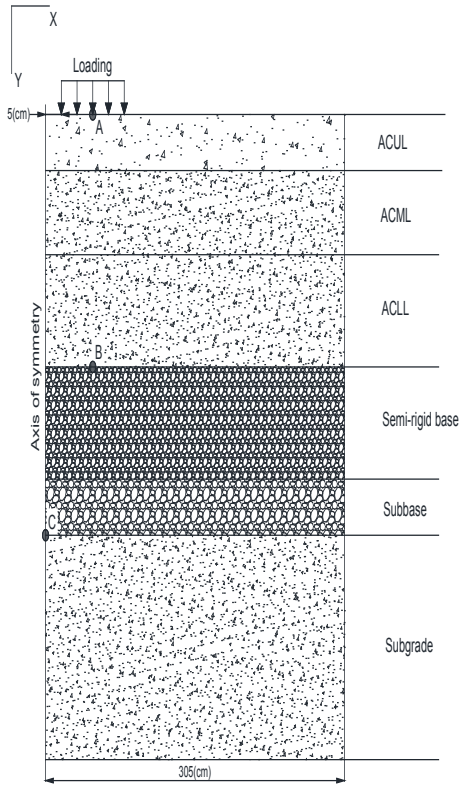

Figure 1. Mesh of pavement structure and monitoring points (Not to scale).

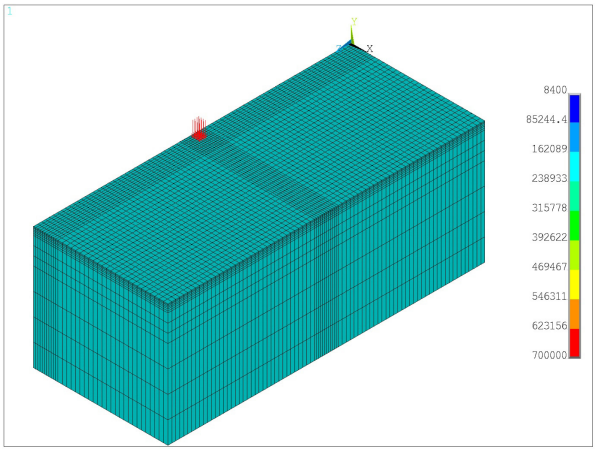

Figure 2. The finite element model of the pavement structure.

2.2 Material characterization

Asphalt mixture has the characteristics of viscoelastic material, and its responses are mainly affected by two factors. One is environment temperature, and the other is loading frequency. Therefore, the dynamic modulus master curve can be utilized for the characterization of the behavior of viscoelastic material, and also used to reflect the performance and behaviors of asphalt concrete. Generally, dynamic modulus $|E^*|$ and phase angle φ are measured by test [18], and they satisfy the following equations:

$$\begin{cases} E^* = E' + iE'' \\ |E^*| = \sqrt{(E')^2 + (E'')^2} \\ E' = |E^*|\cos\varphi,\ E'' = |E^*|\sin\varphi \\ \tan\varphi = E''/E' \end{cases} \tag{2}$$

where $i = \sqrt{-1}$ = unit imaginary number. E' is storage modulus, and E'' is loss modulus. In this research, the dynamic modulus master curve of the asphalt mixtures is constructed by the Modified Havriliak–Negami (MHN) model [18,19], where the loading frequency and environment temperature are taken into account, and it has the following form:

$$E^*(\omega) = E_0 + \frac{E_\infty - E_0}{\left[1 + \left(\frac{\omega_0}{i\omega}\right)^\alpha\right]^\beta} \tag{3}$$

where ω means angular frequency. E_0 is complex modulus when ω approaches 0, and E_∞ is complex modulus when ω approaches ∞. ω_0 is related to the time-temperature shifting and controls the horizontal position of the master curve. α and β are all parameters of the MHN model. Based on the time-temperature superposition principle (TTSP), the influences of loading frequency and environment temperature can be merged into one variable, and this is reduced frequency ω_r, which is defined as follows:

$$\omega_r = \omega \times \alpha_T \tag{4}$$

where α_T is time-temperature shift factor. The Williams-Landel-Ferry (WLF) equation is the most common model for the time-temperature shift factor of asphalt concrete, where α_T is a function of temperature T, as follows:

$$\alpha_T = \frac{-C_1(T-T_0)}{C_2+(T-T_0)} \tag{5}$$

C_1 and C_2 are two parameters of the equation. T_0 denotes reference temperature. Then the dynamic modulus of material at different temperatures can be obtained from the equation of the master curve by replacing the physical frequency with the reduced frequency at the reference temperature, as follows:

$$E^*(\omega,T)=E^*(\omega_r,T_0) \tag{6}$$

The MHN model coefficients of three kinds of asphalt mixture used in this paper are presented in **Table 1**, and the datum is from the reference [18]. It chooses 25 °C as the reference temperature, and the reduced frequency is 5 Hz, which is the typical frequency induced by a truck travelling at 80 km/h on asphalt pavement [11,20].

Compared with the normal temperature, asphalt pavement is more prone to form deformation and damage with the high temperature. Because the material properties of asphalt concrete are related to the environmental temperature. Therefore, the responses of the asphalt pavement structure will be considered at the normal and high temperatures in this research respectively. To obtain the dynamic modulus of each sublayer of asphalt concrete layer at different temperatures, the temperature of each sublayer must be determined first. It is assumed that the temperature of each sublayer of the asphalt concrete layer is changing with the depth of the pavement, and then the empirical formula (7) is used to estimate the temperature of three sublayers of asphalt concrete layer at the high temperature [6]:

$$T = 54.32 + 0.78T_{air} - 0.0025\mathrm{Lat}^2 - 15.14\lg(H+25) \tag{7}$$

where T means the estimated value of the temperature of each structural layer (°C). T_{air} denotes the mean value of maximum temperature within one week (°C). Lat represents the latitude of the area where the asphalt pavement is located (°), and H means the depth of the sublayer from the top of the surface course (mm). Take Xi'an city (in China) as an example, then $T_{air}=36$ (°C, in Summer), $\mathrm{Lat}=34$ (°). Now the temperature of the three sublayers of the asphalt concrete layer in Summer can be determined according to Equation (7). In **Table 2**, the related material parameters of asphalt pavement structure are listed, and the responses of the pavement will be computed at the normal temperature and the high temperature for analyzing the performance of the asphalt pavement.

2.3 Bonding model between adjacent layers

The bonding condition between adjacent layers of asphalt pavement has an obvious influence on the stress transmission and energy dissipation of pavement structure [21], and also affects the prediction of structural responses of asphalt pavement. Therefore, the interlayer condition between adjacent layers is considered to be the interlayer contact bonding condition (ICB condition) in the study, and the interlayer contact bonding model (ICB model) is introduced to simulate realistic interface behavior [17]. The ICB model can be illustrated in **Figure 3**, where the bottom of ACUL cover with contact elements, and the top of ACML is covered with target elements. Spring elements are used to connect the contact elements and the target elements by the corresponding nodes. Meanwhile, other contact interfaces of adjacent layers are all connected in the same way, and then there are totally five contact interfaces as shown in **Figure 3**.

In the ICB condition, the stress is calculated by the contact algorithm according to the length of compression or tension of springs at the corresponding nodes [22]. Each spring has three characteristic parameters, and these parameters are usually created automatically with a contact algorithm on the basis of the mesh size of the finite element and the relevant parameters of material characteristics. But sometimes these parameters need to be adjusted to get a better and convergent solution.

Table 1. The model coefficients of asphalt mixture.

Type	E_0 (MPa)	E_∞ (MPa)	α	β	ω_0	C_1	C_2
SMA13	51.1	26317	0.266	1.693	657.1	21.7	183.5
Sup20	104.8	32128	0.257	1.733	407.9	15.3	139.0
Sup25	35.9	24558	0.296	1.504	612.0	23.1	191.4

Table 2. Material parameters of asphalt pavement structure.

Layer	Normal temperature (°C)	High temperature (°C)	Modulus (MPa)	Poisson's ratio	Density (kg/m^3)	Thickness (cm)
ACUL(SMA13)	20	54(*H*=20)	Determined from master curve	0.30	2350	4
ACML(Sup20)	20	49(*H*=70)		0.30	2360	6
ACLL(Sup25)	20	46(*H*=140)		0.30	2370	8
Base	-	-	1200	0.25	2300	40
Subbase	-	-	300	0.35	1932	20
Subgrade	-	-	50	0.40	1926	200

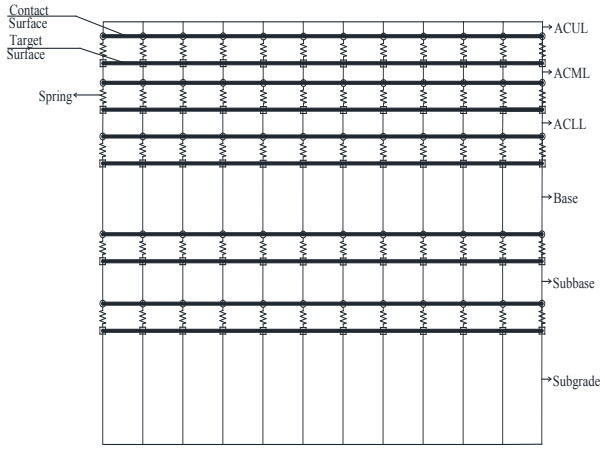

Figure 3. Schematic of ICB model.

In the ICB model, the augmented Lagrangian method is used to calculate the contact stress in the normal and tangential direction [22], and the tangential stress at the contact interface satisfies the following relation:

$$\tau_{\lim} = \mu P + b \tag{8}$$

$$|\tau| \le \tau_{\lim} \tag{9}$$

where $\tau_{\lim}$ is ultimate stress in a tangential direction, μ denotes the coefficient of sliding friction, P means the normal compressive stress, b represents the adhesion stress of the contact interface; τ is the shear stress in the tangential direction. In Equation (8), if μ equals zero or P equals zero, b is not zero, adjacent layers may keep sticking state and no sliding. If b equals zero, this means that there is no bond stress between adjacent layers or adjacent layers appear bond failure. If inequality (9) holds, namely $|\tau|$ is less than or equals $\tau_{\lim}$, the adjacent layers still keep sticking state. Otherwise, there will be relative sliding between adjacent layers. Five contact interfaces are created in **Figure 3**, where the adhesion stress is 0.45 MPa in the three upper interfaces [23], and the adhesion stress is all 0.01 MPa in the other two lower interfaces.

Due to constructional deficiency or the chronic and repeated action of environment and traffic, bond failure between adjacent layers may occur during the service life of asphalt pavement and form the disengaging area. The ICB model can simulate the variation of interlayer bonding conditions by adjusting the value of b. If the bond failure occurs somewhere between the adjacent layers, b in Equation (8) is 0 in disengaging area and unchanged in other areas. In order to facilitate the simulation and calculation, there are five types of disengaging areas to imitate the phenomenon of bond failure,

and they were shown in **Figure 4**. The dashed box in **Figure 4** all means the load region on the surface of ACUL. The shaded area denotes the disengaging area under the load region, and it means that the phenomenon of the local bond failure occurs at the contact interface. In type "T0", the disengaging area is 0, and this means that the adjacent layers keep good bonding condition and no disengaging area appear between the two adjacent layers. In type "T1", the disengaging area is 10×9 cm^2 under the load region, and this denotes that the disengaging area between two adjacent layers is 10 cm in length and 9 cm in width. In type "T2", the disengaging area is 20×18 cm^2 under the load region, and it is the same size as the load region on the surface of ACUL. Besides, types "T3" and "T4" have a similar meaning to the type "T2", but the size of the disengaging area is bigger than the size of the type "T2".

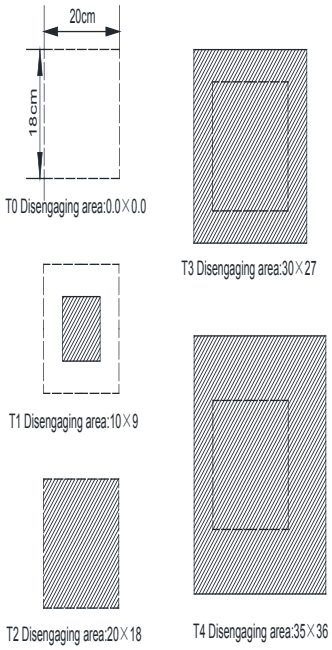

Figure 4. Type of disengaging area under loading area (Not to scale, Unit: cm^2).

2.4 Pavement life prediction method

For the purpose of discussing the effect of interlayer conditions of adjacent layers and temperature on the responses of the asphalt pavement structure, four cases are considered as follows:

Case 1: the interlayer conditions of adjacent layers are the full-bonded condition at the normal temperature.

Case 2: the interlayer conditions of adjacent layers are the full-bonded condition at the high temperature.

Case 3: the interlayer conditions of adjacent layers are the ICB condition at the normal temperature.

Case 4: the interlayer conditions of adjacent layers are the ICB condition at the high temperature.

The axle load number and the rut depth will be predicted to reflect the performance of asphalt pavement. Firstly, assuming that the calculated deflection is equal to the designed deflection, the axle load number of the asphalt pavement within the design service life can be calculated according to the following equation [24,25]:

$$N_e = \left(\frac{600}{k \times l_d}\right)^5 \tag{10}$$

where N_e is the cumulative equivalent single axle loads number of a lane within design service life; k is a coefficient, and the recommended value for it is 1.0; l_d is the designed deflection (0.01 mm).

In order to get the deformation of the pavement structure, the accumulated rut depth (RD) in the entire asphalt pavement can be expressed in the following equation [26]:

$$\mathrm{RD} = \sum_{i=1}^{N} h^i \varepsilon_p^i \tag{11}$$

where RD means the permanent deformation of the asphalt pavement; N denotes the number of sublayers; h^i is the thickness of sublayer i; ε_p^i is the plastic strain in sublayer i. The strain ε_p^i in each of the pavement sublayers can be calculated by the vertical strain ε_z^i, and the relationship is as follows:

$$\frac{\varepsilon_p^i}{\varepsilon_z^i} = k_1 \times 10^{k_2} T^{1.5606} N_{cy}^{0.4791} \tag{12}$$

$$k_1 = (C_1 + C_2 \times dh) \times 0.328196^{dh} \tag{13}$$

$$C_1 = -0.1039 \times h_{ac}^2 + 2.4868 \times h_{ac} - 17.342 \tag{14}$$

$$C_2 = 0.0172 \times h_{ac}^2 - 1.7332 \times h_{ac} + 27.428 \tag{15}$$

where k_1 is the function of h_{ac} and dh; h_{ac} is the thickness of the total asphalt layers (in); dh is the depth from the surface (in); k_2 is calibration factor, and the recommended value for it is −3.79016; T

and N_{cy} are the temperature (°F) and the axle loads number respectively.

3. Response results and analysis

The responses of the pavement structure are computed by the different interlayer conditions and two kinds of temperature conditions, and these responses are applied to forecast the structural performance of asphalt pavement.

3.1 Structural responses with different interlayer condition

The structural responses are computed with the four cases mentioned before, and the results are listed in **Table 3**. The negative value denotes compressive response, and the positive value indicates tensile response. The responses of the three monitoring points with the full-bond condition are smaller than their responses with the ICB condition whether it is normal temperature or high temperature. Compared the responses in case 1 with the responses in case 3 (at the normal temperature), the U_{YA}, ε_{XB} and ε_{ZB} in case 1 are all a little greater than them in case 3, but the ε_{YC} in case 1 is obviously greater than it in case 3. Compared the responses in case 2 with the responses in case 4 (at the high temperature), the U_{YA} in case 2 is a little bigger than it in case 4, but the strain ε_{XB}, ε_{ZB} and ε_{YC} in case 2 are obviously bigger than them in case 4. Regardless of whether it is the normal temperature or the high temperature, the strain ε_{YC} at the top of the subgrade with the full-bond condition is significantly smaller than it is with the ICB condition. It may imply that the way of calculating the responses of asphalt pavement applying with the full-bond condition is possible to underrate the real responses of the asphalt pavement. In addition, the strain ε_{XB} and the strain ε_{YC} in case 2 are comparable with the results obtained by Xue Z. et al. [27], which indicate that the responses calculated by the ICB condition are basically reasonable and acceptable.

Table 3. Responses under different interlayer condition.

Case	U_{YA} (mm)	ε_{XB} (10^{-6})	ε_{ZB} (10^{-6})	ε_{YC} (10^{-6})
Case 1 ①	–0.1669	18.802	39.101	–82.186
Case 2 ②	–0.4894	40.310	55.016	–124.430
Case 3 ③	–0.1691	19.656	40.342	–101.056
Case 4 ④	–0.5068	87.771	106.547	–153.511
Ratio (((③ – ①)/①)*100%)	1.36%	4.55%	3.17%	22.96%
Ratio (((④ – ②)/②)*100%)	3.56%	117.74%	93.66%	23.37%

Assuming that the designed deflection equals the calculated deflection, then the cumulative numbers of the equivalent axle load at the normal temperature can be calculated by Equation (10), and the results are shown in **Figure 5(a)**. The cumulative numbers of the equivalent axle load in case 3 are smaller than those in case 1. It means that the ICB condition reaches the calculated deflection in advance compared with the full-bond condition. The predicted rut depth at the high temperature with one million of the equivalent axle load is shown in **Figure 5(b)**, and the rut depth in case 4 is greater than it in case 2. This denotes that the deformation of asphalt pavement with the ICB condition is more serious than it with the full-bond condition. Based on the above results, it's easy to know that by contrast with the structural responses under the ICB condition, the structural responses of the asphalt pavement with the full-bond condition are relatively small, or the real structure responses of the asphalt pavement are underestimated with the full-bond condition. It may be a good and proper cause to explain the reason for the early diseases of the asphalt pavement structure. Therefore, in the following sections, the ICB model will be applied to estimate the structural responses of the asphalt pavement with different conditions.

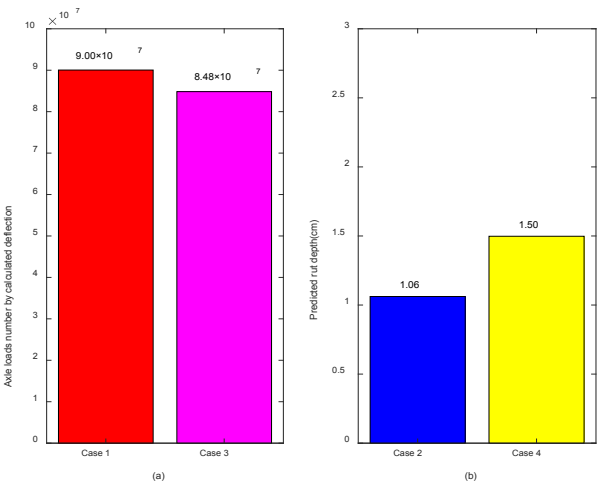

Figure 5. (a) Axle load numbers at the normal temperature and (b) rut depth of asphalt pavement at the high temperature.

3.2 Strains of the asphalt pavement structure under the ICB condition

The strain profile of the asphalt pavement structure is plotted by 56 points at the top of each structure layer, which ranges from 0 m to 0.55 m along the X-axis direction. Because the asphalt pavement structure is symmetrical about the Y axis, the structural responses of asphalt pavement on both sides can be plotted. **Figures 6(a) and (b)** present the strains of the asphalt pavement at the normal temperature, where ε_X is the transverse strain and ε_Z is the longitudinal strain. The longitudinal strains are in compression at the top of the surface course, and the transverse strains under the load position are also in compression. The transverse strains in other positions are very small and approach 0, and this reflects that the semi-rigid base has a strong supporting role in the asphalt concrete surface. The longitudinal strains are in tension at the bottom of the surface course, and the transverse strains under the load position are also in tension. The transverse strains in other positions are in compression. As shown in **Figure 6(b)**, the longitudinal strain ε_Z and transverse strain ε_X at the bottom of the semi-rigid base are all in tension, and the longitudinal strain ε_Z is less than the transverse strain ε_X at the same nodes. ε_Y is the vertical strain at the top of the subgrade, which is all negative, and this means that the subgrade is under pressure.

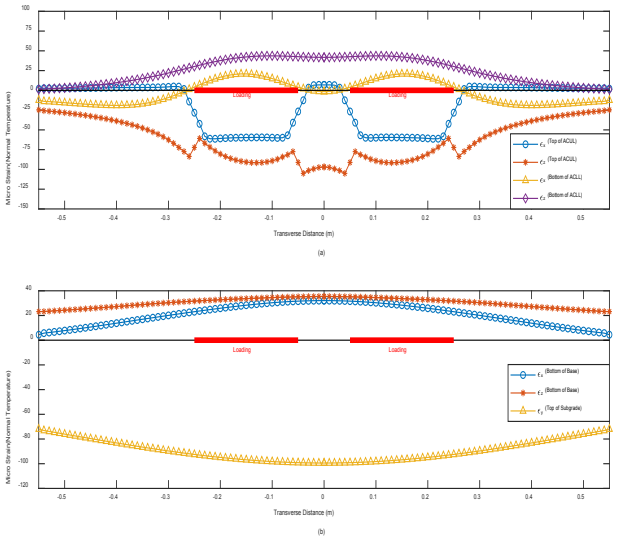

Figure 6. Strains of asphalt pavement at the normal temperature.

Figures 7(a) and (b) present the strains of the asphalt pavement at high temperatures. At the top of the surface course, the longitudinal strains are in compression, and the transverse strains under the loading position are also in compression. However, compared with the normal temperature, the transversely tensile strains at the top of the surface course change remarkably outside the edges of the dual tire, which are bigger than the transversely tensile strain at the bottom of the surface course. At the bottom of the surface course, the longitudinal strains are in tension, and the transverse strains under the loading position are also in tension, but the transverse strains in other positions are in compression. In **Figure 7(a)**, the transversely tensile strain at the top of the ACUL is greater than the strains at the bottom of the ACLL, which is similar to the trend obtained by Alae et al. [11], and the maximum of it reaches almost 460 micro strains.

From **Figures 6(b) and 7(b)**, the strains at normal and high temperatures have a similar trend. In **Figure 7(b)**, the transverse strains ε_X and the longitudinal strains ε_Z at the bottom of the semi-rigid base are almost in tension, and they are slightly larger than that at the normal temperature. The vertical strains ε_Y at the top of the subgrade are all in compression, which has an obvious increase compared with the

normal temperature. According to these results, it is easy to understand that the tensile strains at the top of the surface course with the high temperature may be the main reason for the top-down cracking, and this implies that the transversely tensile strains will be prone to cause the surface course to crack in the traffic direction (longitudinal direction) at the high temperature. This keeps consistent with the research results of Alae et al. [11], and is also basically the same as the conclusion of the classic model of top-down cracking.

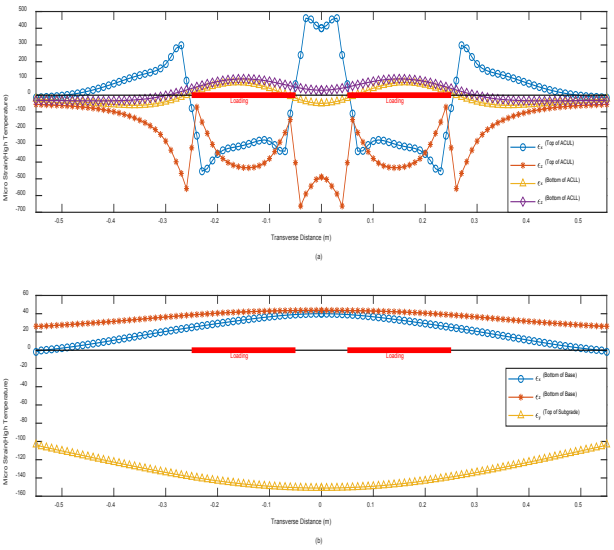

Figure 7. Strains of asphalt pavement at the high temperature.

3.3 Structural responses of asphalt pavement with local bond failure

For purpose of imitating the phenomenon of the local bond failure between two adjacent layers, two cases of bond failure are considered as follows:

Case 1: The local bond failure happens between the ACUL and ACML.

Case 2: The local bond failure happens between the ACLL and the semi-rigid base.

The disengaging area is used to denote the region of the local bond failure, and the five types of the disengaging area as shown in **Figure 4** are considered in this research. The responses of the three monitoring points as shown in **Figure 1** are computed when the different types of the disengaging area happened in Case 1 and Case 2. The results at the normal and high temperatures are listed in **Table 4** and **Table 5** respectively.

In **Table 4**, the responses have an obvious difference in Case 1 and Case 2, and they all keep rising when the disengaging area increases. From type "T0" to type "T4", the increment of the displacement U_{YA} in Case 1 is a little bigger than it is in Case 2, and the strain ε_{YC} has a slight increase in Case 1 and Case 2. However, the increment of the strain ε_{XB} in Case 2 is greater than it in Case 1, and the strain ε_{ZB} have the same trend as the strain ε_{XB}.

Although the responses in **Table 5** are larger than the responses in **Table 4** in the corresponding cases, they have a similar trend. From **Table 4** and **Table 5**, the variation of the displacement U_{YA} in case 1 is greater than that of the displacement U_{YA} in Case 2 at the normal temperature or the high temperature, which means that the influence of Case 1 on the displacement U_{YA} is relatively obvious compared with that of Case 2. The strain ε_{YC} has little change at the normal or high temperature, and this means the local bond failure has a little effect on it. But the strain ε_{XB} and the strain ε_{ZB} all increase observably in Case 1 and Case 2 as the size of disengaging area enlarges, especially in Case 2. It indicates the local bond failure between the bottom of the ACLL and the top of the semi-rigid base has a significantly negative impact on the tensile strains at the bottom of the ACLL, and this will be more serious with the high temperature. Hence, bottom-up cracking may be easy to form when the phenomenon of bond failure occurred between the ACLL and the semi-rigid base. In addition, compared with the interlayer bond failure between the ACUL and the ACML, it is easy to know that the influence of the local bond failure between the ACLL and the semi-rigid base on the strains at the bottom of the surface course is more obvious.

Table 4. Responses with bond failure at the normal temperature.

	Type	U_{YA} **(mm)**	ε_{XB} **(10^{-6})**	ε_{ZB} **(10^{-6})**	ε_{YC} **(10^{-6})**
Case 1	T0 ①	–0.1691	19.656	40.342	–101.056
	T1	–0.1692	19.668	40.360	–101.057
	T2	–0.1709	20.890	41.669	–101.074
	T3	–0.1723	22.852	44.312	–101.147
	T4 ②	–0.1727	23.049	45.198	–101.267
Ratio (((② – ①)/ ①)*100%)		2.13%	17.26%	12.04%	0.21%
Case 2	T0 ③	–0.1691	19.656	40.342	–101.056
	T1	–0.1691	19.952	41.055	–101.053
	T2	–0.1693	24.844	49.339	–101.090
	T3	–0.1697	27.151	54.195	–101.556
	T4 ④	–0.1706	29.219	58.047	–102.014
Ratio (((④ – ③)/ ③)*100%)		0.89%	48.65%	43.89%	0.95%

Table 5. Responses with bond failure at the high temperature.

	Type	U_{YA} (mm)	ε_{XB} **(10^{-6})**	ε_{ZB} **(10^{-6})**	ε_{YC} **(10^{-6})**
Case 1	T0 ①	–0.5068	87.771	106.547	–153.511
	T1	–0.5074	87.930	106.702	–153.511
	T2	–0.5308	97.610	116.280	–153.530
	T3	–0.5445	112.435	131.298	–153.652
	T4 ②	–0.5461	112.826	131.784	–153.838
Ratio (((2–1)/1)*100%)		7.75%	28.55%	23.69%	0.21%
Case 2	T0 ③	–0.5068	87.771	106.547	–153.511
	T1	–0.5068	92.260	115.710	–153.515
	T2	–0.5077	171.619	243.444	–153.580
	T3	–0.5112	202.647	307.269	–154.251
	T4 ④	–0.5158	223.442	351.672	–155.061
Ratio (((④ – ③)/ ③)*100%)		1.78%	154.57%	230.06%	1.01%

3.4 Structural responses of asphalt pavement under moving loads

To estimate the performance of the pavement structure with the moving loads, the structural responses of the three monitoring points as shown in **Figure 1** are computed with vehicle load passing through the surface of ACUL under different speeds. The path length of the moving loads is 720 cm in total, and the moving loads will go 9 cm forward in every iteration. When the moving loads along the traffic direction complete the load path, the iterative process ends. The responses of the three monitoring points are computed at the normal and high temperatures respectively, and the speed of the moving loads is assumed at 30 km/h, 60 km/h, 90 km/h and 120 km/h respectively.

The structural responses shown in **Figures 8(a)-**

(d) are under the condition of normal temperature, and the structural responses shown in **Figures 9(a)-(d)** are under the condition of high temperature. The extremums of the displacement U_{YA} decrease with the increase of vehicle speed whether it is the normal temperature or the high temperature. Furthermore, the value of the displacement under a moving load is basically consistent with Zhao Y. et al. [28] in amount and magnitude, which shows that the response with the ICB model under the moving load is credible. The strain ε_{XB} and the strain ε_{ZB} all have a course of compression, tension and compression, meanwhile, the maximum of the strain ε_{XB} and the strain ε_{ZB} all decrease with the vehicle speed increasing.

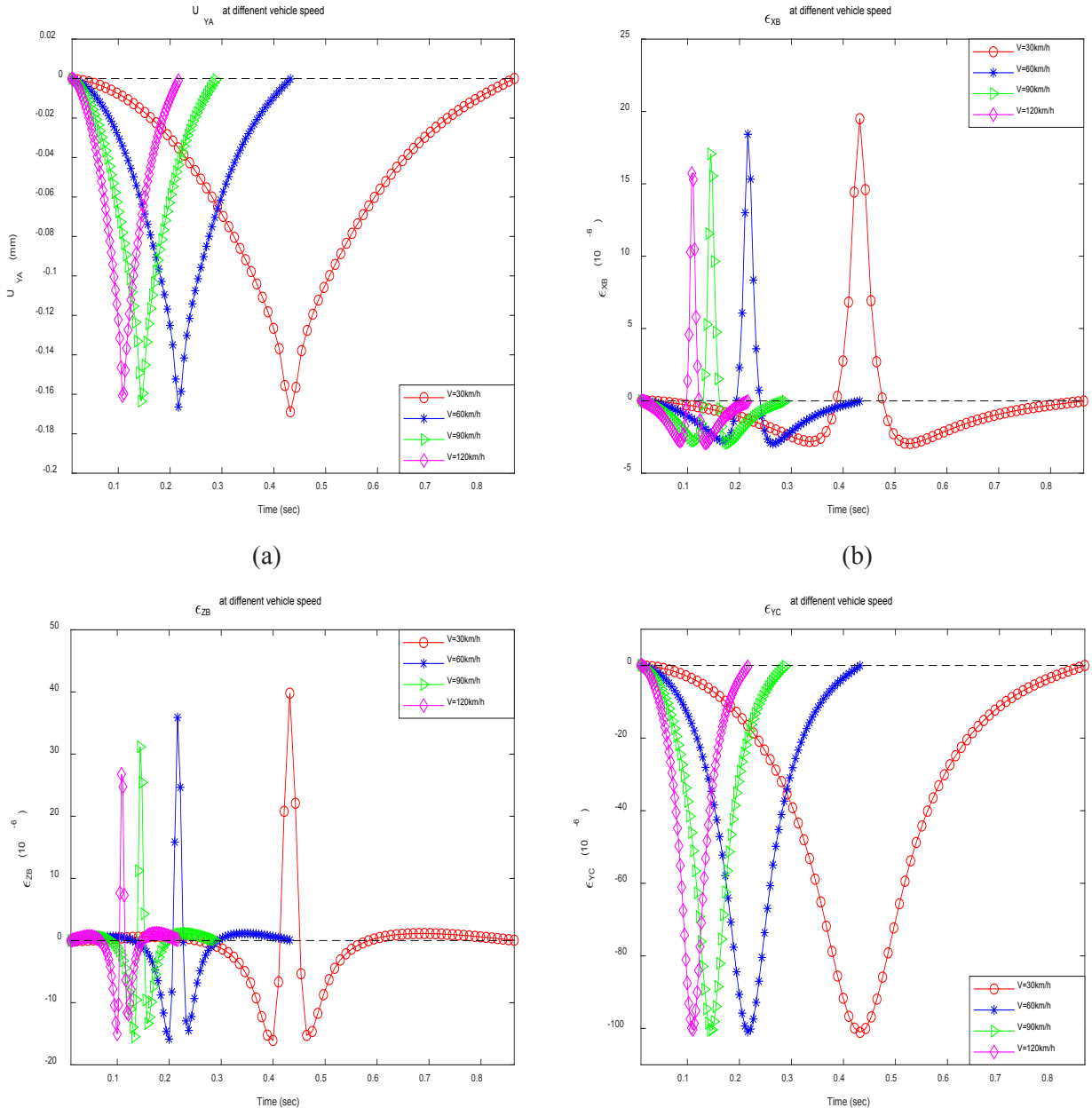

Figure 8. Response due to moving loads at the normal temperature.

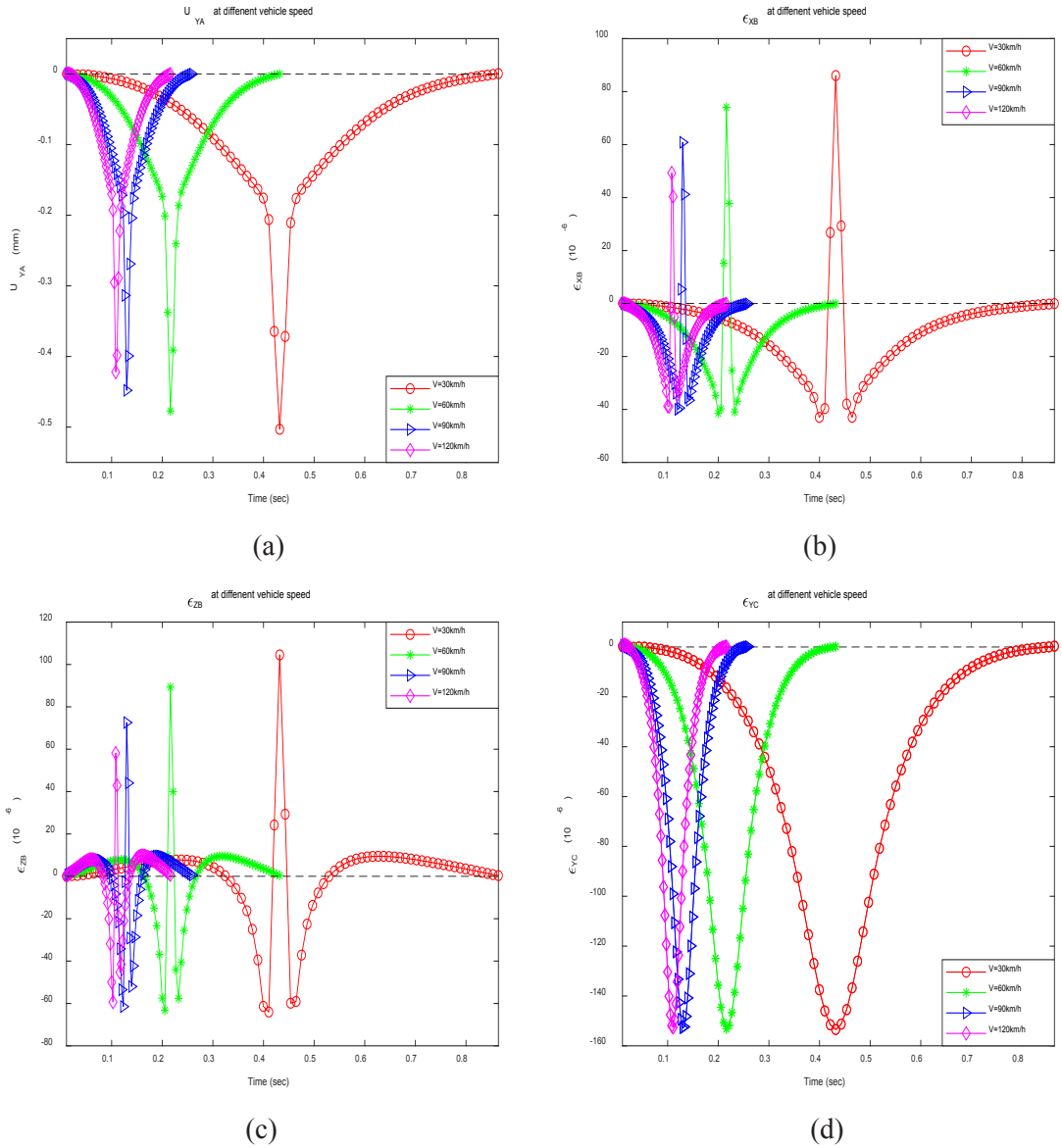

Figure 9. Response due to moving loads at the high temperature.

As vehicle speed increases from 30 km/h to 90 km/h at the normal temperature, the maximum of the strain ε_{XB} and the strain ε_{ZB} decrease by 12.46% and 21.70% respectively. As vehicle speed increases from 30 km/h to 90 km/h at a high temperature, the extreme the strain ε_{XB} and the strain ε_{ZB} decrease by 29.29% and 30.54% respectively. It may indicate that the deformation of asphalt pavement has a strong relationship with the loading time. The strain ε_{YC} under different speeds keeps almost same in the magnitude and trend at normal or high temperatures, and the extreme of the strain ε_{YC} is nearly the same under different speeds in **Figure 8(d)** or **Figure 9(d)**. It indicates that the vehicle load can be effectively transferred to the subgrade by the semi-rigid base. Furthermore, the structural responses of the surface course with the high temperature are significantly bigger than those with the normal temperature, which implies that the structural responses of asphalt pavement also have a strong relationship with the temperature of structural layers. In addition, the trends of structural responses at different vehicle speeds keep in correspondence with that obtained by Alae et al. [19]. So the material performance of asphalt concrete needs to be improved to resist the deformation at high temperatures.

4. Conclusions

The interlayer condition of structural layers of asphalt pavement not only has an effect on the absorption and dispersion of the external loads, but also is of great significance for accurately estimating the structural responses and performance of asphalt pavement. For simulating the interface condition of adjacent layers, the interlayer contact bonding model is applied to achieve the connection mode at the contact interface. To predict the structural behaviors of asphalt pavement with vehicle loads and consider the materials characteristics of asphalt pavement, the structural responses of asphalt pavement are computed with the interlayer contact bonding model at two different temperatures in this research. Furthermore, the structure responses to the local bond failure of the adjacent layer are also studied and the responses of pavement structure with the moving loads are also analyzed. Finally, some conclusions are presented as follows:

(1) Compared with the normal temperature the transversely tensile strains at the top of the surface course are easy to cause top-down cracking at the high temperature outside the edges of the dual tire. Because the influence range of vehicle loads is finite, a critical location for the formation of top-down cracking is the vicinity of the tire edge.

(2) The occurrence of the local bond failure between the ACLL and semi-rigid base breaks the integrality of the pavement structure and weakens the bonding strength between the ACLL and semi-rigid base, which makes the strains at the bottom of the ACLL increase with the increase of the disengaging area, especially at the high temperature. This may promote the chance of the initiation of the down-top cracking, hence, a strong bonding condition between the ACLL and the base needs to be constructed to restrain the occurrence of bond failure and resist the external loads together.

(3) The structural responses have a similar trend with the different vehicle speeds at normal or high temperatures. Although the extreme responses of the pavement structure decrease with the vehicle speed increasing, the asphalt pavement is still vulnerable to form deformation and damage at the interaction of lower speed and higher temperature. Therefore, it is necessary to reasonably limit the vehicle speed and further improve the material performance of asphalt concrete at high temperature.

Conflict of Interest

There is no conflict of interest.

Funding

This research was supported by the Scientific Research Program Funded by Shaanxi Provincial Education Department (Program No.21JK0830) and Shaanxi Provincial Natural Science Foundation Research Project (Program No.2022JM-166).

References

[1] Chun, S.Y., Kim, K., Greene, J., et al., 2015. Evaluation of interlayer bonding condition on structural response characteristics of asphalt pavement using finite element analysis and full-scale field tests. Construction and Building Materials. 96, 307-318.

[2] Kim, H., Arraigada, M., Raab, C., et al., 2011. Numerical and experimental analysis for the interlayer behavior of double-layered asphalt pavement specimens. Journal of Materials in Civil Engineering. 23(1), 12-20.

[3] Ozer, H., Al-Qadi, I.L., Wang, H., et al., 2012. Characterisation of interface bonding between hot-mix asphalt overlay and concrete pavements: Modelling and in-situ response to accelerated loading. The International Journal of Pavement Engineering. 13(2), 181-196.

[4] Zhang, Y., Wang, X., 2012. Impact of condition on mechanical response of asphalt pavement. Journal of Chang'an University (Natural Science Edition). 32(5), 7-11.

[5] Wu, S., Chen, H., Zhang, J., et al., 2017. Effects of interlayer bonding conditions between semi-rigid base layer and asphalt layer on mechanical responses of asphalt pavement structure.

International Journal of Pavement Research & Technology. 10(3), 274-281.

[6] Luo, Y., Zhang, Z., Zhang, K., 2018. Sensitivity analysis of influence factors on shear stress of asphalt pavement under high temperature. Engineering Journal of Wuhan University. 51(10), 895-900.

[7] Zhang, J., Wu, S., Pel J.Z., et al., 2014. Analysis of mechanical responses of asphalt pavement interlayers based on shear spring compliance. Journal of Highway and Transportation Research and Development (English Edition). 8(1), 1-6.

[8] Wellner, F., Hristov, B., 2015. Numerically supported experimental determination of the behavior of the interlayer bond in asphalt pavement. Transportation Research Record Journal of the Transportation Research Board. 2506, 116-125.

[9] Lazar, M.L., Diaconu, E., 2016. Influence of the interface conditions on flexible pavement structures life. Romanian Journal of Transport Infrastructure. 5(1), 30-37.

[10] Cao, D., Zhao, Y., Fu, G., 2017. Influence on the surface dynamic viscoelastic deflection of interlayer bonding condition. Journal of Beijing University of Technology. 43(4), 600-605.

[11] Alae, M., Zhao,Y., Zarei, S., et al., 2018. Effects of layer interface conditions on top-down fatigue cracking of asphalt pavements. International Journal of Pavement Engineering. 21(1), 1-9.

[12] Sun, L., Wang, G., Zhang, H., et al., 2018. Initiation and propagation of top-down cracking in asphalt pavement. Applied Sciences. 8(5), 1-14.

[13] Ashtiani, R.S., Morovatdar, A., Licon, C., et al., 2019. Characterization and quantification of traffic load spectra in texas overweight corridors and energy sector zones: Final report. Technical Report. doi: 10.13140 /RG.2.2.34611.78880.

[14] Morovatdar, A., Ashtiani, R., Licon, C., et al., 2019. Development of a mechanistic approach to quantify pavement damage using axle load spectra from south Texas overload corridors. Geo-Structural Aspects of Pavements, Railways, and Airfields (GAP 2019), Colorado Springs, CO, USA.

[15] Hu, X., Sun, L., 2005. Measuring tire ground pressure distribution of heavy vehicle. Journal of Tongji University(Natural Science). 33(11), 1443-1448.

[16] Dong, H., 2012. Asphalt pavement top-down cracks in laboratory test. Chang'an University, Xi'an, Shaanxi.

[17] Wang, X., Ma, X., 2020. Responses of semi-rigid base asphalt pavement with interlayer contact bonding model. Advances in Civil Engineering. (3), 1-13.

[18] Zhao, Y., Liu, H., Bai, L., et al., 2013. Characterization of linear viscoelastic behavior of asphalt concrete using complex modulus model. Journal of Materials in Civil Engineering. 25(10), 1543-1548.

[19] Alae, M., Zhao, Y., Leng, Z., 2020. Effects of ageing, temperature and frequency-dependent properties of asphalt concrete on top-down cracking. Road Materials and Pavement Design. (4), 1-21.

[20] Al-Qadi, I.L., Wei, X., Elseifi, M.A., 2008. Frequency determination from vehicular loading time pulse to predict appropriate complex modulus in mepdg. Asphalt Paving Technology: Association of Asphalt Paving Technologists-Proceedings of the Technical Sessions. 77, 739-771.

[21] Wang, X., Feng, J., Wang, H., et al., 2018. Effect of the dynamic load on stresses in a deck pavement with an interlayer contact model. Advances in Civil Engineering. (4), 1-10.

[22] Wang, X., Li, Y., Xu, H., 2011. ANSYS structural analysis unit and application. Beijing: China Communications Press.

[23] White, G., 2016. State of the art: Interface shear resistance of asphalt surface layers. International Journal of Pavement Engineering. 18(10), 887-901.

[24] JTG D50-2006, 2006. Specifications for design of highway asphalt pavement. Ministry of Transport of the People's Republic of China.

[25] Zhu, Y., Lei, M., Shi, N., et al., 2011. Influence

of interface condition on structural performance and life prediction of asphalt pavement. Highway Engineering. 36(5), 18-32.

[26] Siddharthan, R.V., Nasimifar, M., Tan, X., et al., 2016. Investigation of impact of wheel wander on pavement performance. Road Materials & Pavement Design. 1-18.

[27] Xue, Z., Wang, C., Zhang, W., et al., 2015. Research on pavement structure and material design of semi-rigid base long-life pavement. Journal of Highway and Transportation Research and Development. 32(10), 37-42,56.

[28] Zhao, Y., Liu, H., Bai, L., et al., 2012. Effect of constitutive relationship of asphalt mixture on pavement response. China Journal of Highway and Transport. 25(5), 6-11.

BILINGUAL PUBLISHING GROUP
Pioneer of Global Academics Since 1984

Journal of Mechanical Materials and Mechanics Research
https://journals.bilpubgroup.com/index.php/jmmmr

ARTICLE

Design and Implementation of a Control System to Mitigate Osteonecrosis in Orthopedic Bone Drilling Procedures

***Kadir Gok*[1], *Yasin Kisioglu*[2], *Arif Gok*[3*]**

[1] *Department of Biomedical Engineering, Engineering and Architecture Faculty, 35665,İzmir Bakircay University, Izmir, Turkey*

[2] *Department of Biomedical Engineering, Kocaeli University, Umuttepe, Kocaeli, 41380, Turkey*

[3] *Department of Industrial Design, Architecture Faculty, Kütahya Dumlupinar University, Kutahya, 43820, Turkey*

ABSTRACT

The drilling process in orthopedic surgery can sometimes lead to an undesired increase in temperature, which can cause serious damage to bones and soft tissues. This overheating is typically identified as a temperature above 47 °C, known as the critical limit, and can result in the condition known as osteonecrosis. This study aims to develop a new control system, using a proportional-integral-derivative (PID) controller, to prevent overheating and the resulting osteonecrosis. The bone temperature is constantly measured using a thermocouple and, when it reaches the critical temperature of 47 °C, the cooling device is activated by the PID-controlled system. This new control system makes the drill machine with cooling device more user-friendly and allows surgeons to set a desired temperature level manually.

Keywords: Bone drilling; Orthopedic surgery; Osteonecrosis; PID controller; Driller mechanism

1. Introduction

Biocompatible medical components are commonly used in orthopedic surgery to heal broken bones. To fix fractures, surgeons use a surgical drill to secure plates with screws, as shown in **Figure 1**. In bone drilling procedures, there is often overheating between the drill and the base material due to high friction, which can cause failures. When the undesired temperature increase exceeds a critical value, it can seriously

*CORRESPONDING AUTHOR:
Arif Gok, Department of Industrial Design, Architecture Faculty, Kütahya Dumlupinar University, Kutahya, Turkey; Email: arif.gok@dpu.edu.tr

ARTICLE INFO
Received: 31 January 2023 | Revised: 7 February 2023 | Accepted: 1 March 2023 | Published Online: 8 March 2023
DOI: https://doi.org/10.30564/jmmmr.v6i1.5435

CITATION
Gok, K., Kisioglu, Y., Gok, A., 2023. Design and Implementation of a Control System to Mitigate Osteonecrosis in Orthopedic Bone Drilling Procedures. Journal of Mechanical Materials and Mechanics Research. 6(1): 16-21. DOI: https://doi.org/10.30564/jmmmr.v6i1.5435

damage the bone and soft tissue in the bone drilling process. This can lead to osteonecrosis, a condition where bones and soft tissue remain anemic due to the failure caused by overheating [1]. There are several studies available in the current literature about the critical value of temperature. Hillery and Shuaib [2] studied and found that bones are seriously damaged when the temperature rises above 55 °C in 30 seconds. Eriksson et al. [3] studied in vivo and presented that the cortical bone of a rabbit exhibited thermal necrosis above 47 °C in 60 seconds. Augustin et al. [4] also reported that the temperature can increase above 47 °C, which can cause irreversible osteonecrosis during the bone drilling process.

Biocompatible medical components are commonly used in orthopedic surgery to heal broken bones. To fix fractures, surgeons use a surgical drill to secure plates with screws, as shown in **Figure 1**. In bone drilling procedures, there is often overheating between the drill and the base material due to high friction, which can cause failures. When the undesired temperature increase exceeds a critical value, it can seriously damage the bone and soft tissue in the bone drilling process. This can lead to osteonecrosis, a condition where bones and soft tissue remain anemic due to the failure caused by overheating. There are several studies in the current literature that examine the critical value of temperature during bone drilling procedures. Hillery and Shuaib [2] found that bones can be seriously damaged when the temperature exceeds 55 °C in 30 seconds. Eriksson et al. [3] studied the effects in vivo and discovered that the cortical bone of a rabbit suffered thermal necrosis when the temperature exceeded 47 °C in 60 seconds. Augustin et al. [4] also reported that temperatures above 47 °C during bone drilling can cause irreversible osteonecrosis.

There are many papers available on bone drilling processes. Papers related to bone structures [3,6-8] and the effects of processing parameters, such as spindle speed and feed rate, drill geometry, have been studied [9-11,4,6]. The processing parameters are extremely important and should be selected at an optimal level because the selection of improper parameters can cause tissue damage [12-15]. The most important of these parameters is the temperature in terms of bone and soft tissues. Many different types of studies are available in the literature to control bone temperature rise. Augustin et al. [16] designed a two-step cooled-drill internally and investigated the increasing bone temperature value.

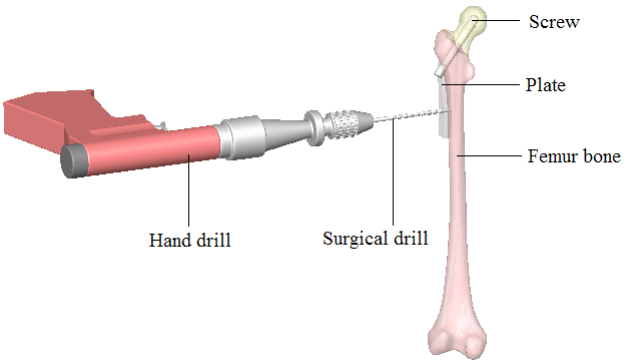

Figure 1. Surgical bone drilling process [5].

The aim of this study is to develop a new control system to control and prevent the undesired temperature rise during the bone drilling process. The new system is developed to control the bone driller mechanism developed in the previous study [5,1]. The bone driller mechanism that was explored previously is having a coolant device that works in a closed-loop to cool the drill bit and bone. The developed new control system is working with Proportional-Integral-Derivative (PID) controller system. The PID system, a kind of sensor or control loop mechanism, is widely used in industrial applications to control the mechanism. The developed PID controller system controls and activates the coolant device of the driller mechanism when the bone temperature rises undesirably. The PID control system is a user-friendly mechanism and surgeons are also able to set up the critical temperature level or desired temperature limit manually. The bone temperature level has been controlled to prevent bone damage caused by overheating.

2. Materials and methods

2.1 Development of PID controller system

The drilling mechanism is composed of three

main components, the drill bit, drill chuck, and closed-loop cooling device, as shown schematically in **Figure 2**. As seen, the drill and drill chuck work together as a combined drilling tool that has cooling devices designed internally in both the drill and drill chuck through hidden cooling slots. The drill bit is mounted on the drill chuck, which is compatible with different diameters of drill bits [5,1].

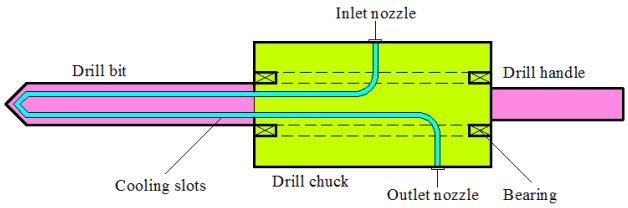

Figure 2. The schematic view of the surgical driller system [5].

The PID control system is developed and inserted into the experimental set to control the coolant device in the case of the bone temperature level rise during the drilling. The developed controller system is mounted to a mini-CNC milling machine for the drilling experiments as seen in **Figure 3**. In the experiments, a thermocouple for temperature measurement and a cooling motor, were switched with a PID controller system to keep the desired bone temperature level. To measure the bone temperature values during the drilling, a thermocouple device has been. These values are saved in the PID controller device as in analog data. During the drilling process, when the bone temperature level reaches the critical temperature value of 47 °C, the cooling system is activated by the controller system. In literature, the critical values of the bone temperatures are variable based on the bone structures but, it is commonly selected as 47 °C, mentioned above. The tissues surrounding the drilled bone are affected when the bone temperature exceeds the critical value so that the desired temperature level can be selected lower by surgeons using the controller system.

The measured temperature value is defined as the peak value (PV) and the desired temperature value is called the set point (SP). When these two values (SP and PV) are compared to each other, the difference between them is called a temperature-error, calculated with Equation (1). Compensating the error is provided by the PID controller equation as given in Equation (2). In order to compensate for the temperature differences, a required Pulse Width Modulation (PWM) is generated by the PID controller system and then the cooling motor is activated instantly. The coolant will be transferred into the chuck and it will circulate through the cooling channels of the surgery drill. The PID controller device will continuously generate the PWM by calculating the error rate. The working system of the PID control system is shown in **Figure 3**. The flowchart of the PID control system is shown in **Figure 4**.

$$e = SP - PV \tag{1}$$

$$U_{PID} = K_p e + K_i \int edt + Kd\left(\frac{de}{dt}\right) \tag{2}$$

where, K_p: Proportion gain, K_i: Integral time constant, K_d: Derivative controller.

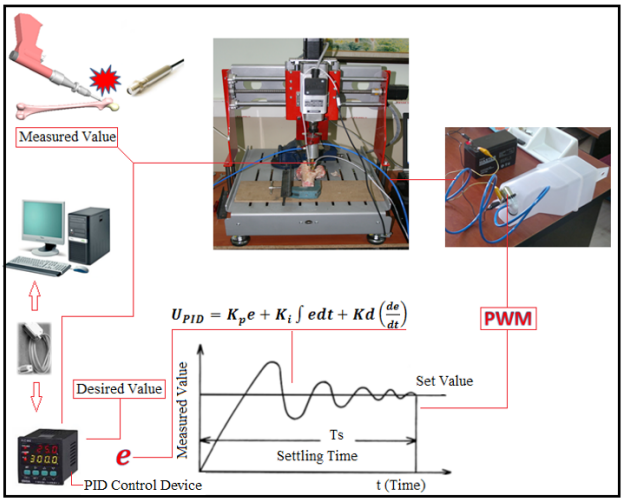

Figure 3. The working system of the PID controller.

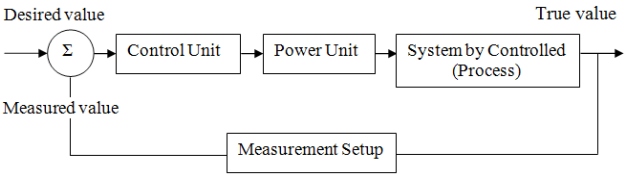

Figure 4. The flowchart of the PID controller system.

3. Results and discussions

The drill bit and cooling system were mounted and fixed on a desktop-type mini CNC milling machine as seen in **Figure 4**. The thermocouple and

cooling motor were clamped and connected to the PID device. The bone drilling processes were performed using the desktop-type mini CNC milling machine. In order to perform the drilling process, a fresh calf femur, a 3-year-old, was used in the mini CNC machine after completing the necessary all samples, tools and equipment. The fresh bone was obtained from a butcher. The bone drilling experiments were performed at a spindle speed (n) of 800 rpm and a feed rate (Vf) of 25 mm/min. When the bone temperature reaches 47 ºC, the PID control system will be activating the cooling motor and system as seen in **Figure 5**. The coolant water is circulated inside the drill bit to cool.

In the drilling experiment of the fresh bovine bone (femur) samples, the drill bit is cutting (drilling) the cortical-cancellous-cortical bones, respectively. The drilling experiments were performed at room temperature conditions using/without the PID controller. During both drilling experiments, the bone temperatures were measured instantly and the results were saved in the computer as in two different curves based on the critical temperature value of 47 ºC. The bone-measured temperatures were plotted as a function of time (sec) shown in **Figure 5**. As seen, the curves are labelled as "No control" and "PID control". Both cortical and cancellous bone temperatures were generally measured lower than 47 ºC when using the PID controller since the cooling system is activated, if necessary, during the drilling process. These measured bone temperatures were shown with the curve named "PID control". As can be seen from the figure, the cancellous and cortical bone temperature was measured after 8.1 seconds slightly higher than the 47 ºC but it is not disturbing.

The spindle speed (n) and feed rate (Vf) are the most important drilling processing parameters to affect bone necrosis. The bone temperature levels that occurred during the drilling can be controlled by the "n" and "Vf". Several papers presented that "rpm" is increasing, and bone temperature is increasing due to overheating on the surgical drill bit or cutting tool [17-19]. The overheating results the bone tissue necrosis. However, the most amount of heat is absorbed by the bone chips that are removed away from the drilling zone. Increasing the "rpm" of the process is accelerating the chip removal from the drilling zone which reduces the bone temperature levels [6,20-25]. Therefore, it is realized that the bone temperature levels during the drilling are depending on the drilling process conditions. The temperatures that occurred in the bone during the drilling can easily be controlled using the developed PID control system.

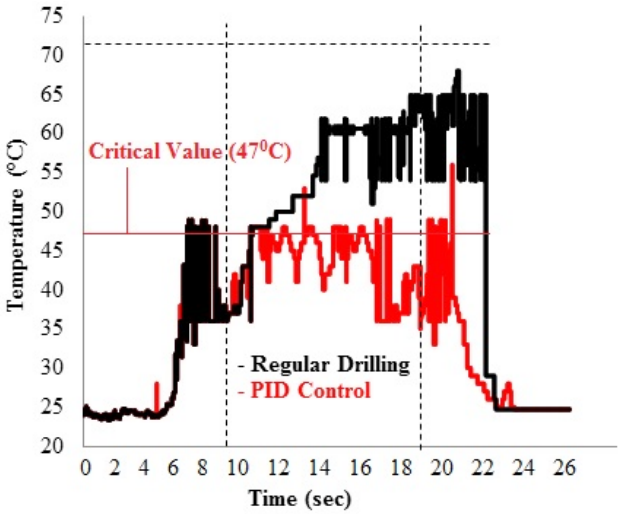

Figure 5. Bone temperatures during bone drilling.

4. Conclusions

In this study, a PID control device/system is developed to control the new driller system developed previous study [5]. The PID control system is controlling and activates the cooling system device and motor of the new driller system when the bone temperatures reach 47 °C during the bone drilling process. In addition, the developed PID controller system is user-friendly since surgeons are also able to set up a critical or desired temperature level manually during the drilling operations. Based on the results obtained in this study, the developed PID controller device is providing a valuable result without osteonecrosis during the bone drilling process at low "rpm".

Acknowledgments

This study was financially supported by the

Department of Scientific Research Project Unit at Kocaeli University under the project number of 2012/44.

Conflict of Interest

There is no conflict of interest.

References

[1] Gök, K., 2014. Drill design and prototype manufacturing to prevent of thermal damage in bone drilling process [PhD thesis]. Kocaeli, Turkey: Kocaeli Üniversity.

[2] Hillery, M.T., Shuaib, I., 1999. Temperature effects in the drilling of human and bovine bone. Journal of Materials Processing Technology. 92-93, 302-308.

[3] Eriksson, A.R., Albrektsson, T., 1984. Heat caused by drilling cortical bone. Temperature measured in vivo in patients and animals. Acta Orthopaedica Scandinavica. 55, 629-631.

[4] Augustin, G., Davila, S., Mihoci, K., et al., 2008. Thermal osteonecrosis and bone drilling parameters revisited. Archives of Orthopaedic & Trauma Surgery. 128(1), 71-77.

[5] Gok, K., Buluc, L., Muezzinoglu, U.S., et al., 2014. Development of a new driller system to prevent the osteonecrosis in orthopedic surgery applications. Journal of the Brazilian Society of Mechanical Sciences and Engineering. 37(2), 549-558.

[6] Toews, A.R., Bailey, J.V., Townsend, H.G.G., et al., 1999. Effect of feed rate and drill speed on temperatures in equine cortical bone. American Journal of Veterinary Research. 60, 942-944.

[7] Martinez, H., Davarpanah, M., Missika, P., et al., 2001. Optimal implant stabilization in low density bone. Clinical Oral Implants Research. 12(5), 423-432.

[8] Chen, H., Sun, J., Hoemann, C.D., et al., 2009. Drilling and microfracture lead to different bone structure and necrosis during bone-marrow stimulation for cartilage repair. Journal of Orthopaedic Research. 27(11), 1432-1438.

[9] Matthews, L.S., Green, C.A., Goldstein, S.A., 1984. The thermal effects of skeletal fixation-pin insertion in bone. The Journal of Bone & Joint Surgery. 66(7), 1077-1083.

[10] Abouzgia, M.B., James, D.F., 1995. Measurements of shaft speed while drilling through bone. Journal of Oral and Maxillofacial Surgery. 53(11), 1308-1315.

[11] Anitua, E., Carda, C., Andia, I., 2007. A novel drilling procedure and subsequent bone autograft preparation: A technical note. International Journal of Oral & Maxillofacial Implants. 22(1), 138-145.

[12] Abukhshim, N.A., Mativenga, P.T., Sheikh, M.A., 2006. Heat generation and temperature prediction in metal cutting: A review and implications for high speed machining. International Journal of Machine Tools and Manufacture. 46(7-8), 782-800.

[13] Mukherjee, I., Ray, P.K., 2006. A review of optimization techniques in metal cutting processes. Computers & Industrial Engineering. 50(1-2), 15-34.

[14] Ueda, T., Nozaki, R., Hosokawa, A., 2007. Temperature measurement of cutting edge in drilling - effect of oil mist. CIRP Annals - Manufacturing Technology. 56(1), 93-96.

[15] Hamade, R.F., Seif, C.Y., Ismail, F., 2006. Extracting cutting force coefficients from drilling experiments. International Journal of Machine Tools and Manufacture. 46(3-4), 387-396.

[16] Augustin, G., Davila, S., Udilljak, T., et al., 2012. Temperature changes during cortical bone drilling with a newly designed step drill and an internally cooled drill. International Orthopaedics (SICOT). 36(7), 1449-1456.

[17] Lee, J., Ozdoganlar, O.B., Rabin, Y., 2012. An experimental investigation on thermal exposure during bone drilling. Medical Engineering & Physics. 34(10), 1510-1520.

[18] Sezek, S., Aksakal, B., Karaca, F., 2012. Influence of drill parameters on bone temperature and necrosis: A FEM modelling and in vitro experiments. Computational Materials Science.

60, 13-18.

[19] Basiaga, M., Paszenda, Z., Szewczenko, J., et al., 2011. Numerical and experimental analyses of drills used in osteosynthesis. Acta of bioengineering and biomechanics. Wroclaw University of Technology. 13(4), 29-36.

[20] Natali, C., Ingle, P., Dowell, J., 1996. Orthopaedic bone drills - can they be improved? Temperature changes near the drilling face. Journal of Bone & Joint Surgery. 78-B(3), 357-362.

[21] Ohashi, H., Therin, M., Meunier, A., et al., 1994. The effect of drilling parameters on bone. Journal of Materials Science: Materials in Medicine. 5(4), 237-241.

[22] Nam, O., Yu, W., Choi, M.Y., 2006. Monitoring of bone temperature during osseous preparation for orthodontic micro-screw implants: Effect of motor speed and pressure. Key Engineering Materials. 321-323, 1044-1047.

[23] Sharawy, M., Misch, C.E., Weller, N., et al., 2002. Heat generation during implant drilling: The significance of motor speed. Journal of Oral and Maxillofacial Surgery: Official Journal of the American Association of Oral and Maxillofacial Surgeons. 60(10), 1160-1169.

[24] Stabler, G.V., 1951. The fundamental geometry of cutting tools. Proceedings of the Institution of Mechanical Engineers. 165, 14-26.

[25] Shamoto, E., Altintas, Y., 1999. Prediction of shear angle in oblique cutting with maximum shear stress and minimum energy principles. Journal of Manufacturing Science & Engineering. 121(3), 399-407.

BILINGUAL PUBLISHING GROUP
Pioneer of Global Academics Since 1984

Journal of Mechanical Materials and Mechanics Research
https://journals.bilpubgroup.com/index.php/jmmmr

ARTICLE

Numerical Solution for Thermal Elastohydrodynamic Lubrication of Line Contact with Couple Stress Fluid as Lubricant

Vishwanath B. Awati[1*], Mahesh Kumar N[1], N.M. Bujurke[2]

[1] *Department of Mathematics, Rani Channamma University, Belagavi, 591156, India*
[2] *Department of Mathematics, Karnatak University, Dharwad, 580003, India*

ABSTRACT

In this paper, the detailed analysis of the influence of thermal and non-Newtonian aspects of lubricant (couple stress fluid) on EHL line contact as a function of slide-roll ratio is presented. The novel low complexity FAS (full approximation scheme), of the multigrid scheme, with Jacobi dipole and Gauss Seidel relaxation is used for the solution of coupled equations viz. modified Reynolds equation, film thickness equation and energy equation satisfying appropriate boundary conditions. The analysis reveals the combined influence of non-Newtonian, thermal and slide-roll ratio (of bearing moving with different speeds) on pressure, film thickness and pressure spike covering a wide range of physical parameters of interest. Results show that pressure spike is strongly influenced by thermal, slide-roll ratio and non-Newtonian character of lubricant with negligible effect on the overall pressure distribution. Also, the minimum film thickness is slightly altered and it increases with the increase in the couple stress parameter. These findings confirm the importance of non-Newtonian and thermal effects in the study of EHL.

Keywords: Thermal EHL; Slide-roll ratio; Couple stress fluid; Multigrid FAS; Non-Newtonian

1. Introduction

Elastohydrodynamic lubrication (EHL) is primarily concerned with the lubrication of contacting surfaces (machine elements) where the high pressure generated, due to high load and speed, in the cavity results in the deformation of (contacting) surfaces. This in turn causes changes in pressure developed and in this process the basic properties of the lubricant are affected. The viscosity and density of the

*CORRESPONDING AUTHOR:
Vishwanath B. Awati, Department of Mathematics, Rani Channamma University, Belagavi, 591156, India; Email: awati_vb@yahoo.com

ARTICLE INFO
Received: 10 January 2023 | Revised: 30 January 2023 | Accepted: 1 March 2023 | Published Online: 15 March 2023
DOI: https://doi.org/10.30564/jmmmr.v6i1.5396

CITATION
Awati, V.B., Mahesh, K.N., Bujurke, N.M., 2023. Numerical Solution for Thermal Elastohydrodynamic Lubrication of Line Contact with Couple Stress Fluid as Lubricant. Journal of Mechanical Materials and Mechanics Research. 6(1): 22-35. DOI: https://doi.org/10.30564/jmmmr.v6i1.5396

lubricant are functions of pressure and temperature. Due to the high speed of contacting surfaces thermal effects will have a considerable influence on EHL lubrication. In the contact region the pressure becomes very large (0.5 GPs to 3 GPs). With large speed film thicknesses reduces to some micrometers and as such wide range of scales is involved in EHL. Dowson and Higginson [1] and periodical review on EHL viz Hamrock and Tripp [2], Dowson and Ehrel [3], Schlijper et al. [4], Spikes [5], Lugt and Morales-Espejel [6] and others provide comprehensive developments (both theoretical schemes and experimental findings) in EHL line as well as point contact problems. Dissertations of Venner [7] and Goodyer [8] and others present many salient features of EHL problems.

The numerical investigation of EHL line contact problems, with Barus viscosity-pressure relation by Petrusevich [9] predicts a second pressure spike near the exit, which is one of the important features of EHL. In the inlet region (considering lubricant flow from left to right) the lubricant is fully flooded, the center (Hertzian contact) is a high-pressure region and again at the exit (out flow) the pressure is zero (cavitation region). Finite difference and finite element methods are commonly used in the EHL investigation. The studies pertaining to a wide range of parameters involved (especially those of high load cases) with algorithms of lower complexity could overcome the limitations of conventional numerical schemes. Okamura [10] presents the numerical solution of isothermal EHL by using the Newton-Raphson method. Lubrecht et al. [11] used a multigrid method introduced by Brandt [12], to solve EHL problems. Later, Brandt and Lubrecht [13] developed MLMI method for the fast evaluation of elastic deformation integral. Full approximation schemes (with Jacobi dipole relaxation) and others played a significant role in easing numerical studies of EHL problems by Venner [14], further details and finer aspects can be found in Venner [7]. Recently, Bujurke et al. [15] used the wavelet preconditioned Newton-GMRES method for the solution of EHL line contact analysis and demonstrate the efficiency of the solver in overcoming the limitations of conventional numerical schemes.

For the pressure and effective modeling of EHL, especially in predicting minimum film thickness, in knowing the spread and height aspects of Petrusevich pressure spike, resulting surface stresses and other aspects of bearing lubrication, it is essential to incorporate the influence of rheology (non-Newtonian nature) of lubricants and thermal effects. Bell [16] was the earliest investigator to predict the importance of lubricant rheology on film thickness using Grubin type method. Houpert and Hamrock [17], Conry et al. [18] solve isothermal EHL equation with Ree-Eyring type lubricant using Newton-Raphson method and cover a wide range of parameters of interest. Jacobson and Hamrock [19] use simplified limiting shear stress model lubricant and find a reduction in film thickness by solving the modified Reynolds equation and film thickness equation simultaneously. Zhu and Neng [20] present theoretical and experimental work on EHL with grease as a lubricant. Bujurke et al. [21] use Jacobian free Netwon-GMRES solver for the solution of EHL line contact problem with grease as a lubricant and present spread and height of Petrusevich pressure spike as a function of a parameter characterizing grease lubricant. Wang et al. [22] use the power law rheological model for the line contact EHL studies under pure rolling and find the location of the cavitation point as a function of the power law exponent. Chippa and Sarangi [23] consider the couple stress fluid model in finite line contact EHL problem and observe that, the increase in film thickness is due to an increase in the couple stress parameter. Das [24] and Saini et al. [25] also use a couple of stress fluid models in their EHL line contact analysis using the conventional finite difference method. Kantli et al. [26] and Shettar et al. [27] use a couple of stress fluid models in their detailed investigation of the second pressure spike and use Jacobian-free Newton-GMRES and Newton-MG schemes respectively. It is of interest to find the entry of bio-based lubricants in EHL[28] which are later also used by Awati et al. [29], Awati and Shankar [30] to find its novel features in tribology. Sternicht et al. [31] were one of the earliest investigators to incorporate thermal effects in EHL

rolling/sliding line contact problem. Later by assuming mean viscosity across the fluid film region, Cheng and Sternicht [32] and Dowson and Whitaker [33] investigate thermal EHL line contact problems for finding minimum film thickness. Murch and Wilson [34], Ghosh and Hamrock [35] attempt in analyzing thermal effects on EHL, which are accurate for moderate parameters (weight and speed). Sadeghi and Sui [36] solve thermal EHL rolling/sliding line contact using a system approach, developed earlier by Houpert and Hamrock [37] and derived accurate film thickness formula. Yang and Wen [38], Wolff et al. [39] analyzed the lubrication problem based on thermal EHL rolling/sliding line contact model and obtained the tapered wedge shape of oil film under high rolling speed and slip conditions. Wolff and Kubo [40] presented the applications of Newton-Raphson method for the solution of thermal EHL line contacts. Hsiao and Hamrock [41], Yang et al. [42] use the combined influence of non-Newtonian and thermal effects on film thickness and surface stresses in EHL line contact problems. Other important studies on this aspect are due to Salahizadeh and Saka [43], over rolling aspects, and recently more effective/detail analysis by Liu et al. [44]. In most of the EHL papers, the solutions of EHL-line contact problems were solved by using Newton-Raphson method. The demerits of Newton-Raphson method are that, the computational complexity of the method is of order $O(n^3)$, n is the number of calculation points in the calculation domain. The elastic deformations term is the Jacobian matrix which is a $n \times n$ matrix and obtaining its inverse requires $O(n^3)$ operations. Also, for high load and high speed the Jacobian becomes singular for a finer grid in employing the Newton-Raphson method. This difficulty can be overcome by using much lower complexity schemes for the solution. In this respect the computation complexity of the FAS method is of order $O(nlogn)$ which is a more efficient method compared to Newton-Raphson.

Multigrid FAS method [45]

The nonlinear system of algebraic equations can be written as $L^h(u^h) = f^h$, where L^h is the nonlinear operator, u is the exact solution, f is the right hand side and h is the mesh size of a uniform finer grid. Let v be an approximation to the exact solution then $e^h = u^h - v^h$ denotes the error and $r^h = f^h - L^h(v^h)$ represents the residue. In FAS, instead of solving the error in the next coarser grid by restricting the residue, the system of nonlinear equations is solved with a modified right-hand side, i.e. $f^{2h} = I_h^{2h} r^h + L^{2h}(I_h^{2h} v^h)$. Continuing this process till the coarsest level H is reached and error is computed as $e^H = u^H - v^H$. This error is added to the solution obtained in the next fine grid by interpolation and relaxation to get a new solution. Error is computed and this process is repeated until the finest level is reached.

The schematic representation of two grid FAS cycle is as follows:

1) Relax $L^h(u^h) = f^h$ with a few relaxations on a fine grid with an initial value u_0^h to get v^h.

2) Compute residue $r^h = f^h - L^h(v^h)$ and restrict residue r^h and v^h to a coarser grid.

3) Compute modified RHS as $f^{2h} = I_h^{2h} r^h + L^{2h}(I_h^{2h} v^h)$ and relax $L^{2h}(u^{2h}) = f^{2h}$ with the initial guess $v^{2h} = I_h^{2h} v^{2h}$.

4) Calculate error $e^{2h} = u^{2h} - v^{2h}$ and interpolate to finer grids and add to v^h.

5) Again relax $L^h(u^h) = f^h$ with v^h to get an approximate solution.

2. Mathematical formulation

Consider two infinitely long cylinders that are rolling at speeds u_1 and u_2, separated by a lubricant (here couple stress fluid) and supporting a load W per/unit axial length. The elastic cylinders are of radius R_1 and R_2 with elastic moduli E_1, E_2 and of Poisson's ratio v_1 and v_2 respectively. As rollers support high loads they experience elastic deformation in the central or Hertz contact region. With usual assumptions [1] the lubricant film thickness in dimensionless form is:

$$H(\mathrm{X}) = \mathrm{H}_0 + \frac{X^2}{2} + \overline{V} \tag{1}$$

where $H_0 = \frac{h_0 R}{b^2}$, $\frac{1}{R} = \frac{1}{R_1} + \frac{1}{R_2}$, b is the half width of

Hertz contact zone, $H=\frac{hR}{b^2}$, h is the film thickness and h_0 is offset film thickness.

$$\overline{V}=\frac{-1}{2\pi}\int_{X_{in}}^{X_{out}}P(X)Log(\mathrm{X-S})^2\,\mathrm{dS} \tag{2}$$

P is dimensionless pressure buildup in the lubricant cavity, X_{in}, X_{out} are inlet and outlet boundary co-ordinates (location) and $X=\frac{x}{b}$.

The dimensionless steady-state Reynolds equation for compressible couple stress fluid as a lubricant is given by Saini et al. [25].

$$\frac{\partial}{\partial X}\left(\frac{\overline{\rho}H^3}{\overline{\eta}\ \xi}\frac{dP}{dX}\right)-K\frac{d}{dX}(\overline{\rho}H)=0 \tag{3}$$

where $\xi=\left[1-\frac{12}{\Omega^2}+\frac{12}{\Omega^3}\tanh\left(\frac{\Omega}{2}\right)\right]^{-1}$, $L_m=\frac{\lambda_a}{R}$, $\Omega=\frac{8WH}{\pi L_m}$, $K=\frac{3U\pi^2}{4W^2}$, L_m is a dimensionless couple stress parameter and λ_a is the molecular length of additive.

The dimensionless load balance equation is:

$$\int_{X_{in}}^{X_{out}}P(X)dX=\frac{\pi}{2}. \tag{4}$$

The Roelands [46] relation, in dimensionless form, connecting viscosity-pressure-temperature is:

$$\overline{\eta}=\exp\left[\left\{\ln(\eta_0)+9.67\right\}\left[-1+\left(1+5.1\times10^{-9}P_HP\right)^{\overline{z}}\right]+\gamma T_0(1-T)\right]. \tag{5}$$

where η_0 is the absolute viscosity, $P_H=\frac{p_h}{p_0}$ is ambient pressure and $\overline{z}$ is a constant characteristic of the liquid (pressure-viscosity index). The modified form of Dowson-Higginson [1] relation about density-pressure-temperature in dimensionless form is:

$$\overline{\rho}=\left[1+\frac{0.6\times10^{-9}P_HP}{1+1.7\times10^{-9}P_HP}\right]\left\{1-\beta T_0(T-1)\right\}. \tag{6}$$

The boundary conditions for the pressure distribution are:

$$P(X_{in})=0;\ \text{and}\ P(X_{out})=\frac{dP}{dX}=0 \qquad at\ \ \mathrm{X}=\mathrm{X}_{out}. \tag{7}$$

Energy equation

Assume the lubricant properties such as thermal conductivity, specific heat and thermal expansivity to be constants with respect to pressure and temperature than the energy equation in dimensionless form is [47]:

$$\frac{\partial^2T}{\partial\overline{Z}^2}=K_3\overline{\rho}H^2\left(\overline{U}\frac{\partial T}{\partial X}\right)-K_2H^2T\left(\overline{U}\frac{\partial P}{\partial X}\right)-K_1\frac{\overline{\eta}}{\phi}\overline{\tau}\left(\frac{\partial\overline{U}}{\partial\overline{Z}}\right) \tag{8}$$

where, $K_1=\frac{(E'RU)^2}{T_0\eta_0k}$, $K_2=\frac{\beta(E'R)^2U}{4\eta_0k}\left(\frac{8W}{\pi}\right)^2$, $K_3=\frac{c\rho_0E'R^2U}{\eta_0k}\left(\frac{8W}{\pi}\right)^{3/2}$ and $\varphi=\frac{\pi U\overline{\eta}}{8WH}$, $u=u_a+\frac{u_b-u_a}{h}z+\frac{1}{2\eta}\frac{\partial p}{\partial x}\left\{z^2-hz+2\lambda_a^2\left[1-\frac{\cosh(2z-h)/2\lambda_a^2}{\cosh(h/2\lambda_a)}\right]\right\}$, from Siani et al [25]. $\overline{\tau}=\frac{\tau}{E'}$ and τ is shear stress of the couple stress fluid and is given by $\tau=\eta\left(\frac{\partial u}{\partial z}-\lambda_a^2\frac{\partial^3u}{\partial z^3}\right)$.

The associated boundary conditions for the energy equation becomes:

$$T(X,0)=T_a;\ \ T(X,H)=T_b \tag{9}$$

where T_a and T_b are the lower and upper surface temperatures of bearing surfaces and are given by [37]:

$$T_a(X)=1+\frac{k_f(\eta_0)^{1/2}(\pi/8W)^{3/4}}{\sqrt{\pi\rho_1c_1k_1[E'U(1-s/2)]R}}\int_{X_i}^{X}\frac{1}{H}\left(\frac{\partial T}{\partial\overline{Z}}\right)_{\overline{Z}=0}\frac{dX'}{\sqrt{X-X'}} \tag{10}$$

$$T_b(X)=1+\frac{k_f(\eta_0)^{1/2}(\pi/8W)^{3/4}}{\sqrt{\pi\rho_2c_2k_2[E'U(1+s/2)]R}}\int_{X_i}^{X}\frac{1}{H}\left(\frac{\partial T}{\partial\overline{Z}}\right)_{\overline{Z}=1}\frac{dX'}{\sqrt{X-X'}} \tag{11}$$

The mean dimensionless temperature T_m is obtained as follows:

$$T_m=\int_0^1Td\overline{Z} \tag{12}$$

In fact, the surface temperatures T_a and T_b (mentioned above) are not known in advance. The heat generated in the lubricant is due to roller surfaces experiencing continuous heat flux from the lubricant film as it moves through the contact area. This temperature rise at the surface of rollers is equivalent to a stationary semi-infinite solid subjected to a moving heat source on its surface which is an elegant work-out problem in Carslaw and Jaeger [48] and this solution is the notation of our boundary conditions on T_a and T_b mentioned above.

3. Discretization of governing equations

The Equations (1)-(3) and (8) are discretized using second-order finite difference approximation with grid size (with a number of grid points N) $N=512$ in the spatial domain of computation i.e.

$[X_{in}, X_{out}]=[-4, 1.5]$ and X_c, the cavitation point to be determined during the solution process. The discretized form of the Reynolds equation and relevant boundary conditions are:

$$\frac{\varepsilon_{i-1/2}P_{i-1}-(\varepsilon_{i-1/2}+\varepsilon_{i+1/2})P_i+\varepsilon_{i+1/2}P_{i+1/2}}{\Delta X^2}=K\frac{\rho_i H_i-\rho_{i-1}H_{i-1}}{\Delta X} \quad (13)$$

where, $\Delta X=X_i-X_{i-1}$, $\varepsilon_i=\frac{\overline{\rho_i}H_i^3}{\eta_i\xi_i}$ and $\varepsilon_{i\pm\frac{1}{2}}=\frac{\varepsilon_i\pm\varepsilon_{i\pm1}}{2}$,

$$P(X_{in})=0 \text{ and } \frac{P(X_{out})-P(X_{out-1})}{\Delta X}=0. \quad (14)$$

The film thickness equation in discretized form as:

$$H_i=H_0+\frac{X_i^2}{2}+\frac{1}{2\pi}\sum_{j=1}^{N}D_{i,j}P_j, \quad (15)$$

where, $D_{i,j}=-\left(i-j+\frac{1}{2}\right)\Delta X\left[\text{h}\left(\left|i-j+\frac{1}{2}\right|\Delta X\right)-1\right]+\left(i-j+\frac{1}{2}\right)\Delta X\right)-1\Big]+\left(i-j+\frac{1}{2}\right)\Delta X\left[\text{h}\left(\left|i-j-\frac{1}{2}\right|\Delta X\right)-1\right]$ for $i=0,1,2,...,N$, $j=0,1,2,...,n$. The force balance equation in discretized form as:

$$\Delta X\sum_{i=1}^{N}\left(\frac{P_i+P_{i-1}}{2}\right)-\frac{\pi}{2}=0 \quad (16)$$

The energy equation in discretized form as:

$$\frac{1}{(\Delta\overline{Z})^2}(T_{k-1}-2T_k+T_{k+1})=K_3\overline{\rho_k}H_i^2\overline{U}_k\left(\frac{T_{i,k}-T_{i-1,k}}{\Delta X}\right)-K_2H_i^2\overline{U}T_k\frac{\partial P}{\partial X}-K_1\frac{\overline{\eta_k}}{\varphi}\overline{\tau}\left(\frac{\partial\overline{U}}{\partial\overline{Z}}\right) \quad (17)$$

The convergence criteria for pressure and temperature becomes:

$$\frac{\sum(P_i^{k+1}-P_i^k)}{\sum P_i^{k+1}}\le\varepsilon \text{ and } \frac{\sum(T_i^{k+1}-T_i^k)}{\sum T_i^{k+1}}\le\varepsilon,$$

where, $\varepsilon=1E-4$ is error tolerance.

4. Numerical method

We use Multigrid Full Approximation Scheme (FAS) for the solution of a nonlinear system of algebraic equations i.e. Equations (13) to (16) with relations Equations (5) and (6). The geometry and material parameters used are the ones given in Saini et al. [25] which pertain to broad aspects of (EHL line contact) bearing in use. The relaxation process in FAS is followed as described by Venner [14]. The coefficient ε in Equation (13) varies several orders of magnitude over the computational domain. The inlet and outlet regions $\varepsilon>>1$ (η and H^3 are large), whereas in contact regions $\varepsilon<<1$ (η and H^3 are relatively small). For $\varepsilon>>1$, Gauss-Seidel relaxation and for $\varepsilon<<1$, Jacobi dipole relaxation is applied with an under-relaxation factor of 0.3~0.6; and 0.1~0.3 respectively.

The procedure of FAS for EHL problem requires pressure correction in every grid but H_0 in load balance is corrected only on the coarsest grid. Let us assume that an approximate solution $\tilde{P}_i$, $\tilde{H}_i$ is obtained from Equation (15). The Gauss-Seidel relaxation process is applied in obtaining new approximation $\overline{P}_i$ in the region of large ε/h^2 and is given by:

$$\overline{P}_i=\tilde{P}_i+\left(\frac{\partial L_i^h}{\partial P_i}\right)^{-1}r_i,$$

where, r_i is the residual of the discrete Reynolds equation at i,

$$r_i=-(\varepsilon_{i-1/2}\overline{P}_{i-1}-(\varepsilon_{i-1/2}+\varepsilon_{i+1/2})\tilde{P}_i+\varepsilon_{i+1/2}\tilde{P}_{i+1})/h^2+(\tilde{\rho}_i\tilde{H}_i-\tilde{\rho}_{i-1}\tilde{H}_{i-1})/h,$$

And $\frac{\partial L_i^h}{\partial P_i}$ is obtained:

i.e. $$\frac{\partial L_i^h}{\partial P_i}\approx-(\varepsilon_{i-1/2}+\varepsilon_{i+1/2})/h^2+\frac{1}{\pi}(\tilde{\rho}_iK_{i,i}^{hh}-\tilde{\rho}_{i-1}K_{i-1,i}^{hh})/h.$$

The Jacobi dipole relaxation process is applied in the region of small ε/h^2 and pressure is updated as $\overline{P}_i=\tilde{P}_i+\delta_i$ and $\overline{P}_{i-1}=\tilde{P}_{i-1}-\delta_i$. For the calculation δ_i we use:

$$\delta_i=\left(\frac{\partial L_i^h}{\partial P_i}-\frac{\partial L_i^h}{\partial P_{i-1}}\right)^{-1}r_i$$

where,

$$r_i=-(\varepsilon_{i-1/2}\tilde{P}_{i-1}-(\varepsilon_{i-1/2}+\varepsilon_{i+1/2})\tilde{P}_i+\varepsilon_{i+1/2}\tilde{P}_{i+1})/h^2+(\tilde{\rho}_i\tilde{H}_i-\tilde{\rho}_{i-1}\tilde{H}_{i-1})/h$$

and,

$$\frac{\partial L_i^h}{\partial P_i}-\frac{\partial L_i^h}{\partial P_{i-1}}\approx-(2\varepsilon_{i-1/2}+\varepsilon_{i+1/2})/h^2+\frac{2}{\pi}(\tilde{\rho}_iK_{i,i}^{hh}-\tilde{\rho}_{i-1}K_{i-1,i}^{hh})/h$$

The cavitation condition is obtained by replacing negative $\overline{P}_i$ values (in the calculation) with zero. There satisfy the load balance equation and H_0 is corrected as:

$$H_0=H_0-c\left(\frac{\pi}{2}-h\sum_{j=0}^{n-1}0.5\left(\overline{P}_j+\overline{P}_{j+1}\right)\right)$$

where c is a suitably chosen constant and $\overline{P}_j$ denotes the current approximation to P_j. The algorithm for the solution of the thermal EHL problem:

1) Solve the Reynolds equation by the FAS

method and apply MLMI method to solve elastic deformation with initial pressure and temperature.

2) Obtained pressure is used to solve energy equation by finite difference with the Gauss-Seidel iteration method.

3) The temperature in step 2) is again used to solve the Reynolds equation for pressure and thermal equation.

4) This process is repeated till convergence is achieved.

5. Result and discussion

Computations are performed using FAS with Jacobi dipole relaxation (Reynolds equation), MLMI (film thickness equation) and Gauss-Seidel (Temperature/heat equation) for various parameters and obtain pressure, film thickness and temperature distributions and details of a pressure spike. By using double precision arithmetic and confining to the stopping criterion of iteration as mentioned above. Profiles of P and H for various L_m with sliding ratio $s=0.5$ and $s=0.1$ are given in **Figure 1(a, b)** for the isothermal case and those in **Figure 2(a, b)** with thermal effect. Pressure in the inlet and Hertz contact region is not much affected by either couple stress or thermal effect. However, the pressure spike with the isothermal case and its influence is found that shift towards centre of the contact region with increasing L_m. These are shown with moderate load and speed for both $s=0.5$ and $s=0.1$. However, film thickness increases with increasing values of L_m for both isothermal and thermal cases. Profiles in **Figure 3(a, b)** are pressure and film thickness for varying load and moderate value of U and L_m with $s=0.5$ and $s=0.1$ respectively. Pressure spike has a noticeable sharp increase in height for $s=0.5$ compared with $s=0.1$. Not much change in other parts of P but there is a slight variation in minimum film thickness with increasing W. Profiles in **Figure 4(a, b)** are again for P and H with varying speed and fixed values of W and L_m for $s=0.5$ and $s=0.1$ respectively. Pressure spike has a marginal effect but film thickness decreases considerably for increasing values of U in both the cases of slide/rolling ratio. A similar observation is made with earlier theoretical models on EHL line contact by Wang and Zhang [47] using different rheological models and Saini et al. [25] a compressible couple stress fluid model. They employ Newton-Raphson method for their analysis of moderate load and moderate speed. The present solver overcomes these limitations and it enables to analyze of the problem by incorporating moderate to high load and high speed.

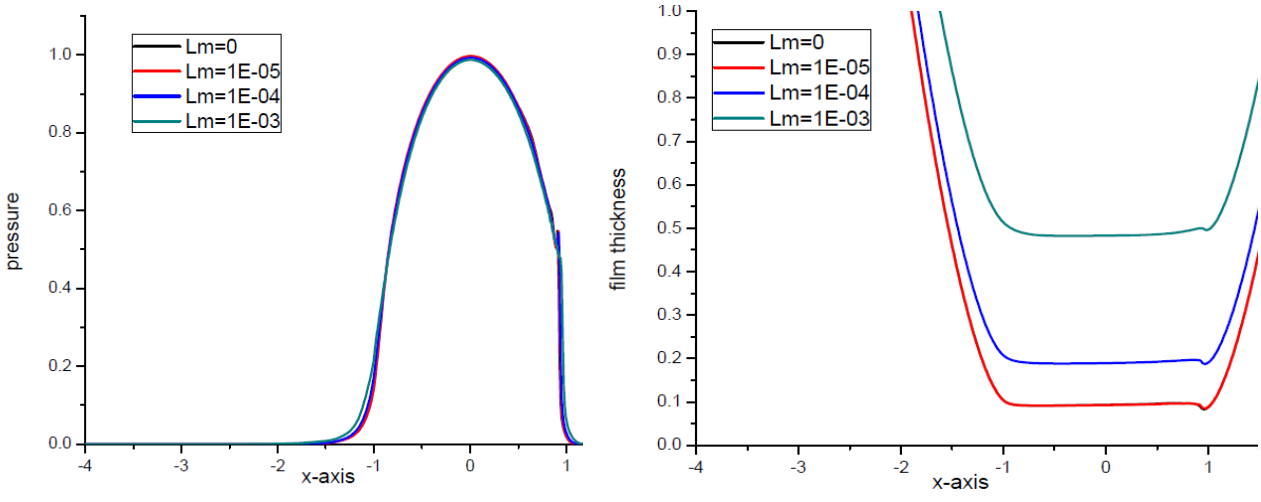

Figure 1a. Isothermal Pressure and film thickness profiles for varying L_m at U=2E-11, W=2E-04 and s=0.5.

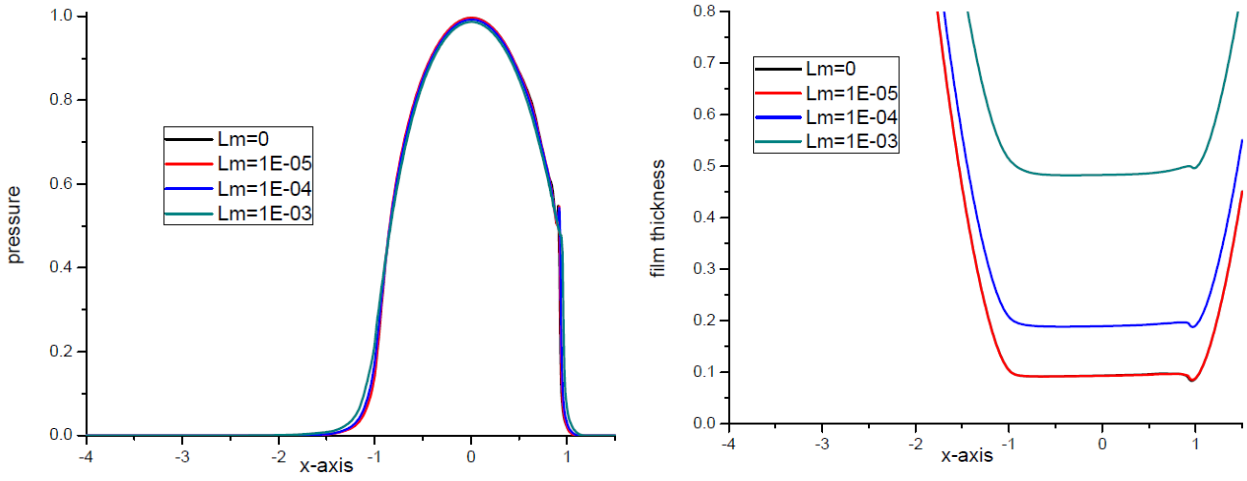

Figure 1b. Isothermal Pressure and film thickness profiles for varying L_m at U=2E-11, W=2E-04 and s=0.1.

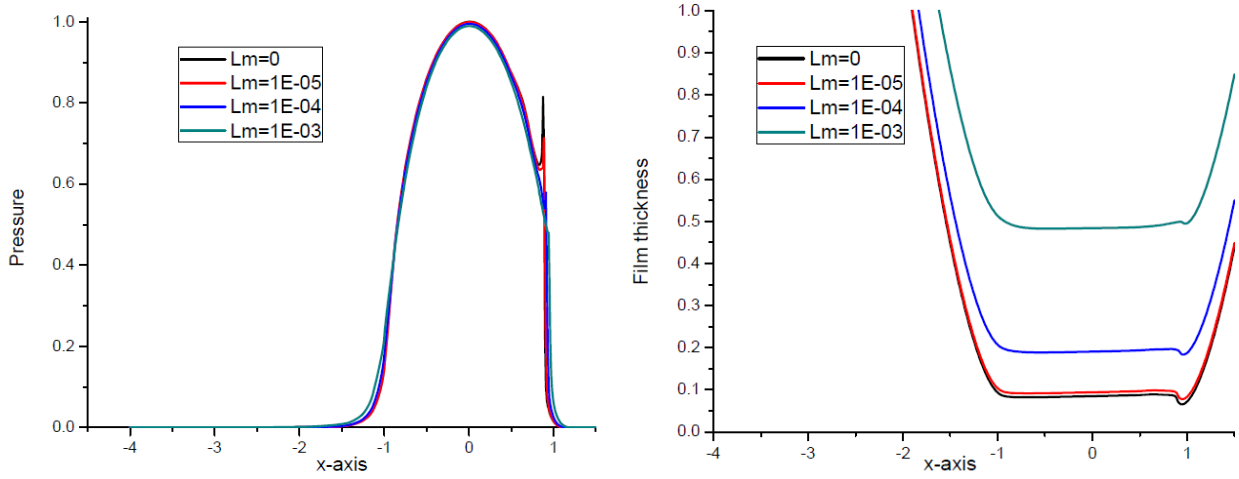

Figure 2a. Thermal pressure and film thickness profiles for varying L_m at U=2E-11,W=2E-04 and s=0.5.

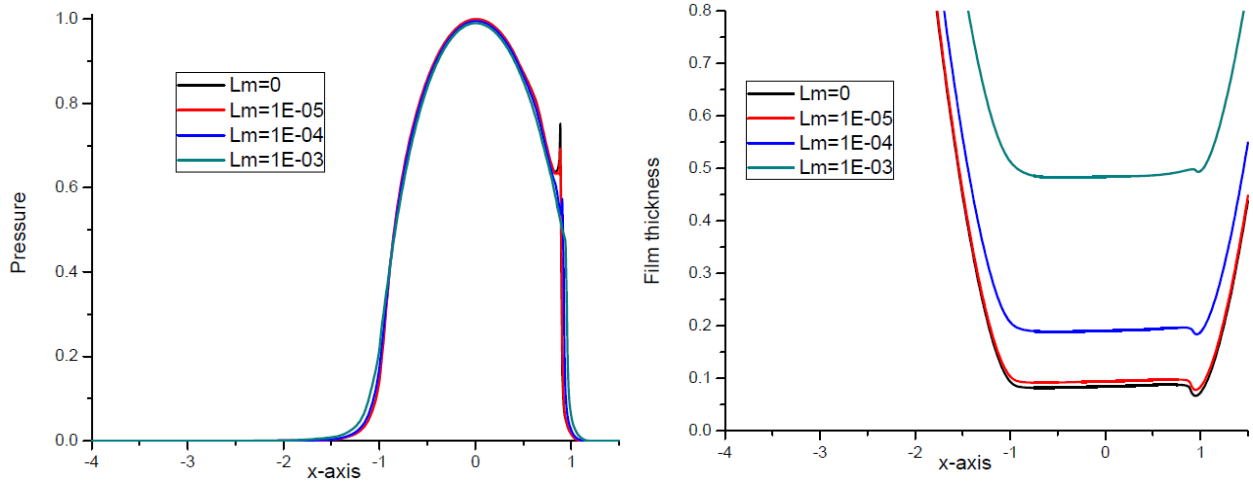

Figure 2b. Thermal pressure and film thickness profiles for varying L_m at U=2E-11,W=2E-04 and s=0.1.

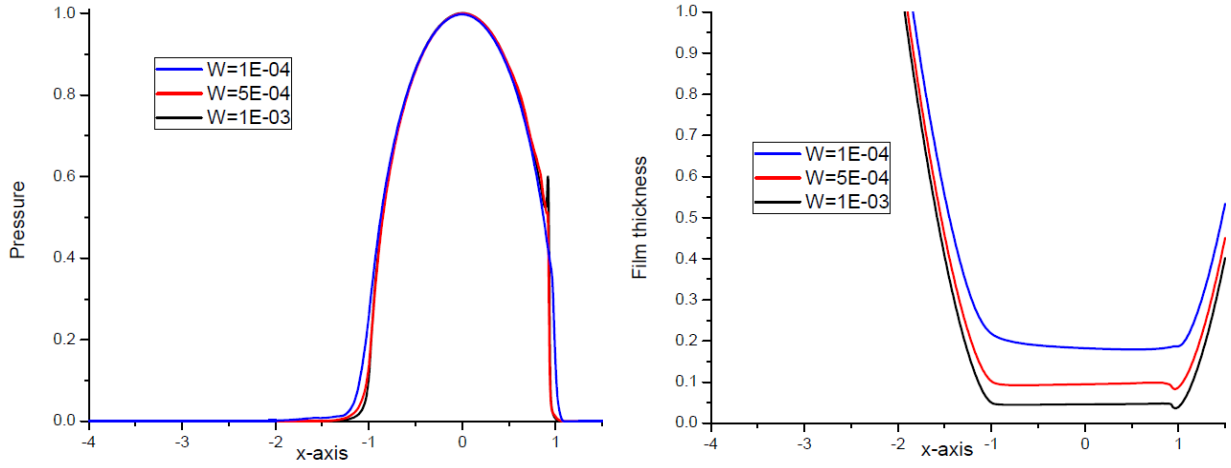

Figure 3a. Thermal pressure and film thickness profiles for varying W at U=2E-11, L_m =1E-04 and s=0.5.

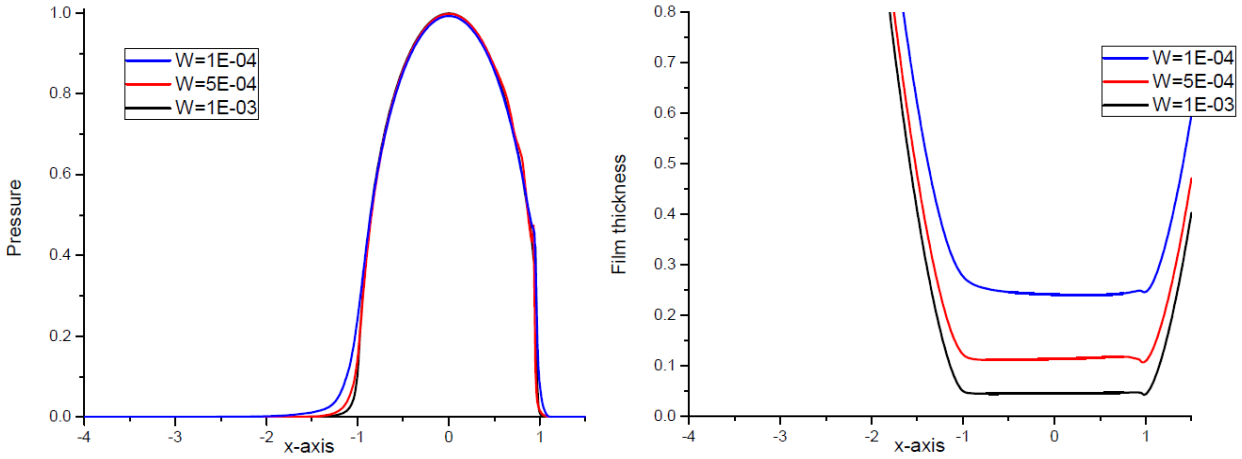

Figure 3b. Thermal pressure and film thickness profiles for varying W at U=2E-11, L_m =1E-04 and s=0.1.

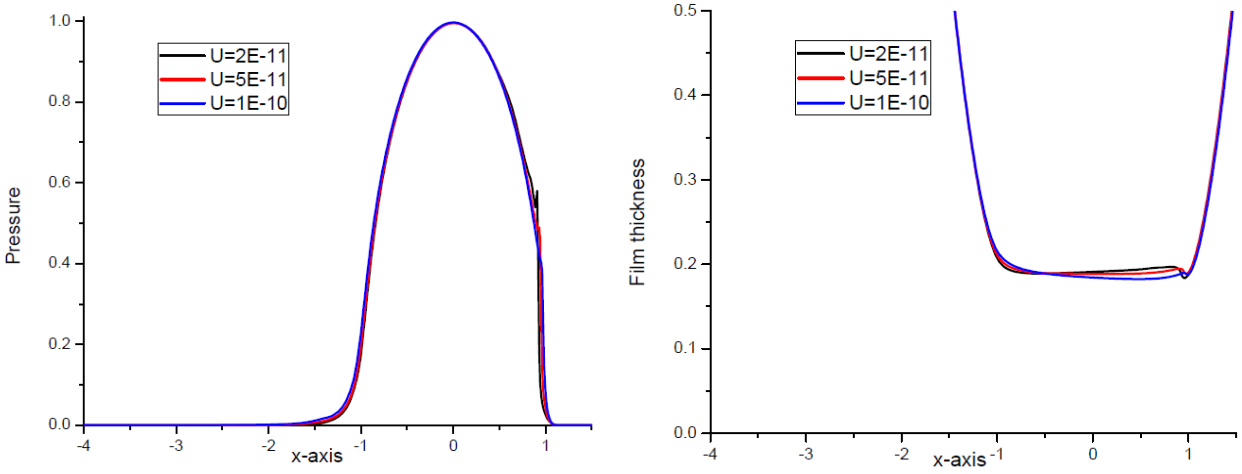

Figure 4a. Thermal pressure and film thickness profiles for varying U at W=2E-04, L_m =1E-04 and s=0.5.

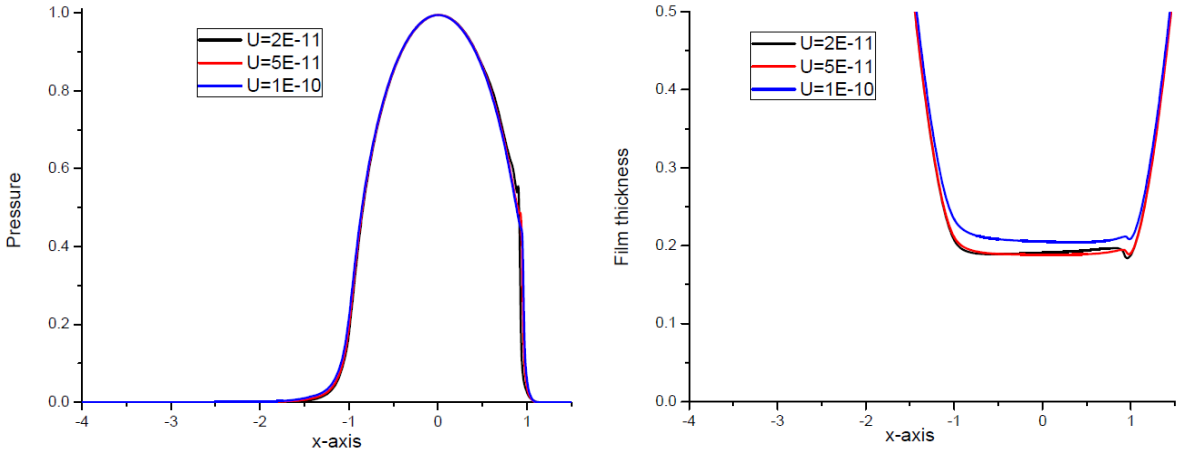

Figure 4b. Thermal pressure and film thickness profiles for varying U at W=2E-04, L_m =1E-04 and s=0.1.

The detailed analysis of pressure spikes is of much importance in bearing design. Earlier attempts on this topic are by Bisset and Glander [49], Venner and Napel [50] and Bujurke et al. [15] using different methods. Here, we present the pressure spike in an enlarged region to elucidate its details. In **Figure 5(a, b)** details of pressure spike (height, spread, location) with varying load and prescribed U and L_m are shown for $s=0.5$ and $s=0.1$ respectively. In Isothermal, case pressure spike decreases for increasing load but using thermal effect it has noticeable height and spread but shifts towards exit region. Much sharper profiles are observed for $s=0.5$ and compared with that of $s=0.1$. In **Figure 6(a, b)** profiles of pressure spikes are shown for varying L_m and fixed moderate W and U for both $s=0.5$ and $s=0.1$ respectively. Spike is spread in a larger region with greater height and it shifts slightly towards the center of the contact for increasing slide/rolling ratio with thermal effect. Spike structure analysis is a delicate issue but we just present our findings, which are qualitative. There is an increase in minimum film thickness with an increase in s compared with viscous lubricant. However, for both viscous and couple stress fluids there is a marginal decrease in minimum film thickness due to thermal effects. From profiles in **Figure 7(a, b)**, it is clear that, the pressure spike increases slightly whereas film thickness decreases considerably for the increase in slide-roll ratio. In **Figure 8** pressure spike in the enlarged region (of **Figure 7a**) is shown. Profiles in **Figure 8** show these assertions clearly.

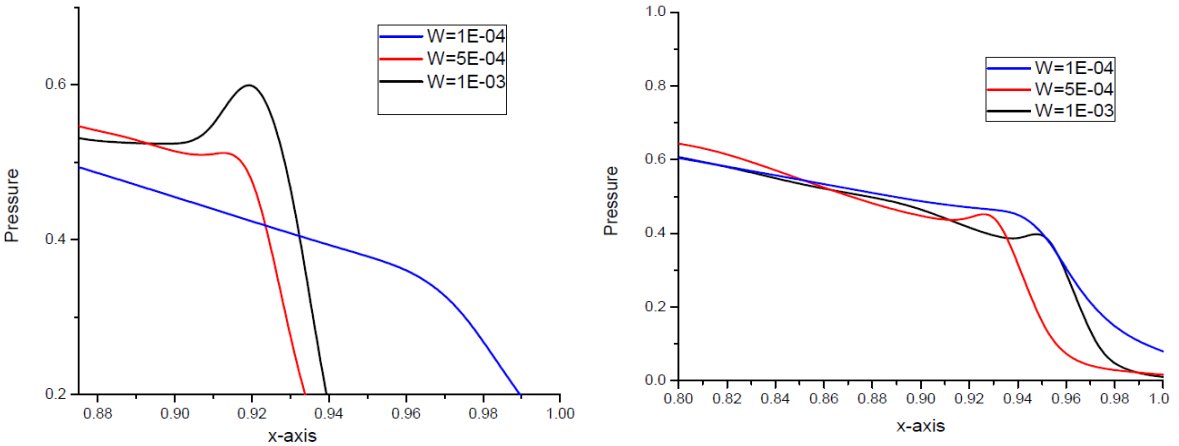

Figure 5. Thermal pressure spike for varying W at U=2E-11, L_m =1E-04, s=0.5(a) and s=0.1(b).

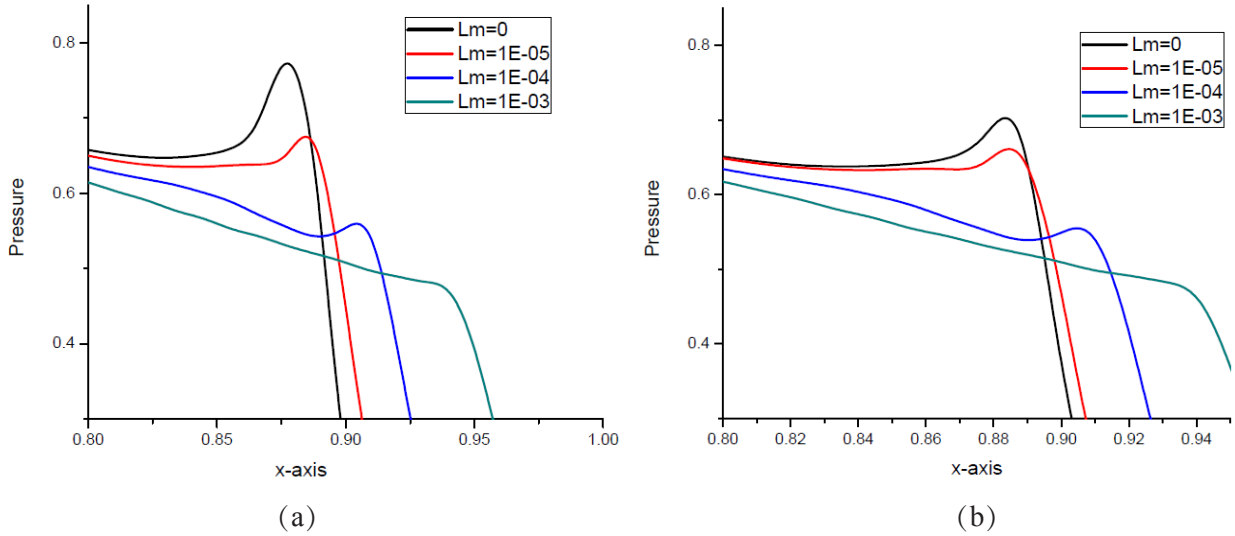

Figure 6. Thermal pressure spike for varying L_m at U=2E-11, W=2E-04, s=0.5(a) and s=0.1(b).

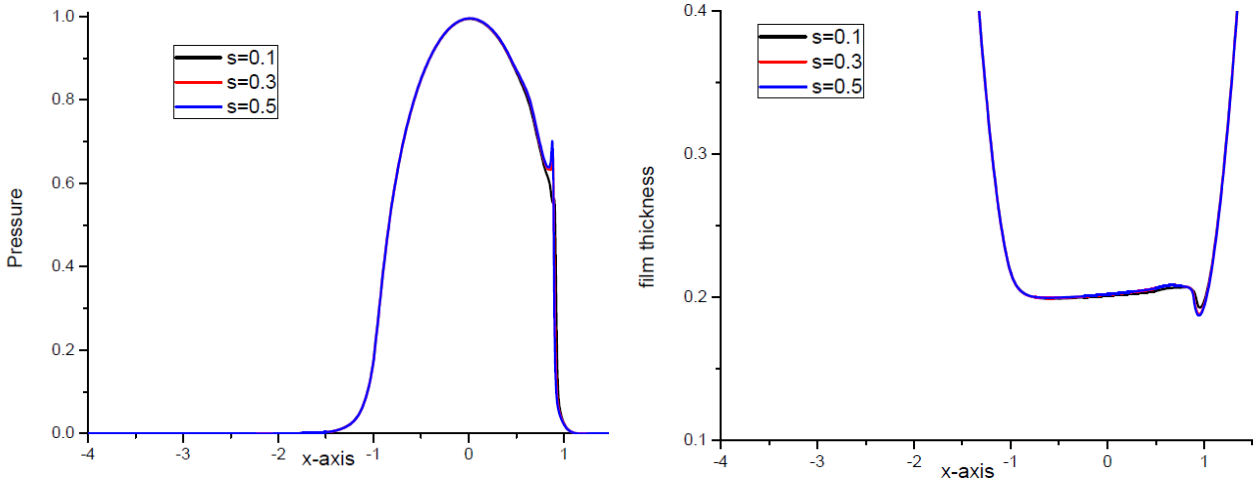

Figure 7(a, b). Thermal pressure and film thickness profile for varying s at U=2E-11,W=2E-04, Lm=1E-4.

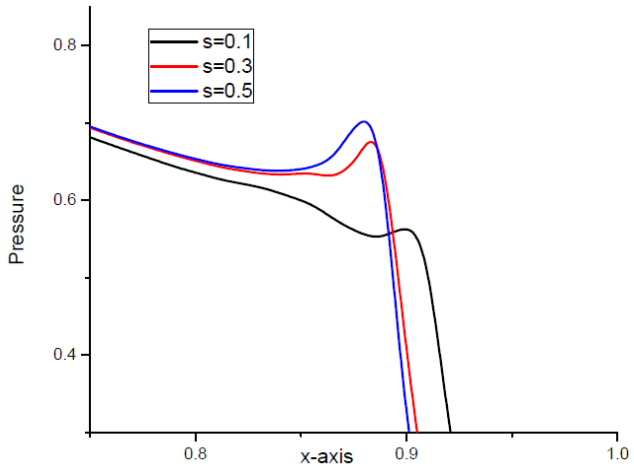

Figure 8. Thermal pressure spike profile for varying s, at U=2E-11, W=2E-04 and *Lm*=1E-04.

6. Conclusions

FAS is one of the most efficient algorithms of low complexity for the analysis of more involved EHL problems, which overcomes the limitation of conventional numerical schemes. The observations such as a decrease in height and spread of pressure spike and shift of its location (or maximum value) towards the center of the contact region for an increase in s, the slide-roll ratio (or moving bearing surfaces), is a useful prediction in design of bearings. Pressure spike increases with increase s, the slide-roll ratio. The rise in temperature decreases with increasing s with couple stress fluid as a lubricant (compared with viscous cases), whereas the pressure spike shifts towards exit for the increase in load and speed and is almost dimensionless in height as well as in spread. Minimum film thickness decreases with thermal effects but with non-Newtonian aspect of the lubricant, minimum film thickness increases with an increase in L_m the couple stress parameter. These predictors can serve as a sort of input information for the bearing designers.

Nomenclature

b half width of the Hertzian contact zone, $b=\left[8wR/(\pi E')\right]^{1/2}$

E' effective elastic modulus of roller and disc, $\frac{1}{E'}=\frac{1}{2}\left(\frac{1-v_1^2}{E_1}+\frac{1-v_2^2}{E_2}\right)$

$E_{1,2}$ elastic modulus of solids

h film thickness

H dimensionless film thickness

L_m couple stress parameter

G material parameter, $G=\alpha E'$

P dimensionless pressure, $\frac{p}{p_H}$

p pressure

p_H maximumHertzian pressure, $p_H=2w/\pi b$

R reduced radius of curvature in the x-direction

t temperature

T_0 inlet temperature of the lubricant

T dimensionless temperature, $T=\frac{t}{T_0}$

U dimensionless speed parameter $U=\eta_0 u_m/(E'R)$

u_m average entrainment speed $u_m=(u_a+u_b)/2$

$u_{a,b}$ lower and upper surface speed.

s sliding/rolling ratio

w applied load per unit length

W dimensionless load parameter $W=w/(E'R)$

α pressure viscosity parameter

X dimensionless-ordinate, $X=\frac{x}{b}$

ΔX space increment

$\overline{Z}$ dimensionless coordinate, $\overline{Z}=\frac{z}{H}$,

$\Delta\overline{Z}$ increment along z axis

Greek symbols

α pressure viscosity index

β thermal—density coefficient

γ thermal-viscosity coefficient of lubricant

$k_{1,2}$ thermal conductivity of rollers

k_f thermal conductivity of lubricant

$\rho_{a,b}$ density of solids

$\upsilon_{1,2}$ Poisson's ratio of solids

τ shear stress

$c_{1,2}$ specific heat of solids

η viscosity of lubricant

η_0 viscosity at ambient pressure

$\overline{\eta}$ dimensionless viscosity

ρ density of lubricant

ρ_0 inlet density of pressure

$\overline{\rho}$ dimensionless density

c_p specific heat of lubricant

λ_a molecular length of additive.

$\overline{\tau}$ $=\frac{\tau}{E'}$

Conflict of Interest

There is no conflict of interest.

References

[1] Dowson, D., Higginson, G.R., 1997. Elastohydrodynamic lubrication, second edition. Pergamon Press: Oxford.

[2] Hamrock, B.J., Tripp, J.H., 1983. Numerical methods and computers used in Elastohydrodynamic lubrication. Proceedings 10th leeds Lyon Symposium, Tribology. Butterworth Scientific Ltd.: London. pp. 11-19.

[3] Dowson, D., Ehrel, P., 1999. Present and future studies in Elastohydrodynamic lubrication. Proceedings of the Institution of Mechanical Engineers Part J-Journal of Engineering Tribology. 213, 317-333.

[4] Schlijper, A.G., Series, L.E., Rycrist, J.E., 1996. Current tools and techniques in EHL modeling. Tribology International. 29(8), 669-673.

[5] Spikes, H.A., 2006. Sixty years of EHL. Lubrication Science. 18, 265-291.

[6] Lugt, P.M., Morales-Espejel, G.E., 2011. A review of Elastohydrodynamic theory. Tribology Transaction. 54, 478-496.

[7] Venner, C.H., 1991. Multilevel solution of the EHL line and point contact problems [PhD thesis]. Netherland: Twente University.

[8] Goodyer, C.E., 2001. Adaptive numerical methods for EHL [PhD thesis]. Leeds: University of Leeds.

[9] Petrusevich, A.I., 1951. Fundamental conclusions from the contact hydrodynamic theory of lubrication. IZV.Akad. Mank, SSSR (Ctal). 2, 209-223.

[10] Okamura, H.A., 1982. Contribution to the numerical analysis of isothermal elastohydrodynamic lubrication. Tribology of reciprocating rngines. Proceedings of the 9th Leeds-Lyon Symposium on Tribology. Butterworth Scientific Ltd.: London. pp. 313-320.

[11] Lubrecht, A.A., Ten Napel, W.E., Bosma, R., 1986. Multigrid, an alternating method for calculating film thickness and pressure profiles in elastodyrodynamically lubricated line contacts. Journal of Tribolgy. 108, 551-556.

[12] Brandt, A., 1984. Multigrid Techniques: 1984, Guide with application to fluid dynamics. GMD Bonn.

[13] Brandt, A., Lubrecht, A.A., 1990. Multilevel matrix multiplication and fast solution of integral equations. Journal of Computational Physics. 90, 348-370.

[14] Venner, C.H., Ten Napel, W.E., Bosma, R., 1990. Advanced multilevel solution of the EHL line contact problem. Transaction of the ASME. 112, 426-432.

[15] Bujurk, N.M., Shettar, B.M., Kantli, M.H., 2017. Wavelet preconditioned Newton-Krylov method for EHL line contact problems. Applied Mathematical Modeling. 46, 285-298.

[16] Bell, J.C., 1962. Lubrication of rolling surfaces by a Ree-Eyring fluid. ASLE Transactions. 5, 160-171.

[17] Houpert, L.G., Hamrock, B.J., 1985. Elastohydrodynamic lubrication calculation used as a tool to study scffing. Proceedings 12th Leeds Lyon symposium on Tribology. Butterworth Scientific Ltd.: London. pp. 146-159.

[18] Conry, T.F., Wang, S., Cusano, C., 1987. A Reynolds-Eyring equation for elastohydrodynamic lubrication in line contacts. Transaction ASME, Journal of Tribology. 109, 648-658.

[19] Jacobson, B.O., Hamrock, B.J., 1984. Non-Newtonian fluid model incorporated into elastohydrodynamic lubrication of rectangular contacts. ASME Journal of Tribology. 106(2), 275-284.

[20] Zhu, W.S., Neng, Y.T., 1988. A Theoretical and experimental study of EHL with grease. Transaction ASME Journal of Tribology. 110, 38-43.

[21] Bujurke, N.M., Shettar, B.M., Hiremath, P.S., 2018. A novel numerical scheme for the analysis of effects of surface roughness on EHL line contact with couple stress fluid as lubricant. Indian Academy of Sciences, Saadhana. 43, 1-22. doi: 10.1007/s12046-018-0906.

[22] Wang, S.H., Hua, D.Y., Zhang, H.H., 1988. A

full numerical EHL solution for the line contacts under pure rolling condition with a Non-Newtonian Rheological Model. Journal of Tribology. 110(4), 583-586.

[23] Chippa, S.P., Sarangi. M., 2013. Elastohydrodynamically lubricated finite line contact with couple stress fluids. Tribology International. 67, 11-20.

[24] Das, N.C., 1997. Elastohydrodynamic lubrication theory of line contacts couple stress fluid model. Tribology Transaction. 40, 353-359.

[25] Saini, P.K., Kumar, P., Tandon, P., 2007. Thermal elastohydrodynamic lubrication characteristics of couple stress fluid in rolling/sliding line contacts. Proceedings of the Institution of Mechanical Engineers—Part J, Journal of Engineering Tribology. 221, 141-153.

[26] Kantli, M.H., Shettar, B.M., Bujurke, N.M., 2017. Jacobian free Newton-GMRES method for analyzing combined effects of surface roughness and couple stress character of lubricant on EHL line contact. INSA. 83, 175-196.

[27] Bujurke, N.M., Kantli, M.H., Shettar, B.M., 2018. Jacobian free Newton-GMRES method for the solution of elastohydrodynamic grease lubrication in line contact using wavelet based preconditioner. Proc. Acad. Sci. A Phy. Sci. 88(2), 247-265.

[28] Awati, V.B., Shankar, N., Mahesh Kumar, N., 2016. Multigrid method for the EHL line contact with bio-based oil as lubricant. Applied Mathematics and Nonlinear Science. 1(2), 359-368.

[29] Awati, V.B., Shankar, N., Mahesh Kumar, N., 2018. Multigrid method for the solution of EHL point contact with bio-based oil as lubricants for smooth and rough asperity. Industrial Lubrication and Tribology. 70(4), 599-611. doi: 10.1108/ILT-12-2016-0314.

[30] Awati, V.B., Shankar, N., 2018. An Isothermal Elastohydrodynamic lubrication of elliptical contact with multigrid method. Australian Journal of Mechanical Engineering. 18(3), 375-384. doi: 10.1080/14484846.2018.1531810.

[31] Sternlicht, B., Lewis, P., Flynn, P., 1961. Theory of lubrication and failure of rolling contacts. ASME Transaction of Tribology. 83, 213-226.

[32] Cheng, H.S., Sternlicht, B., 1965. A numerical solution for the pressure, temperature and film thickness between two infinitely long, lubricated rolling and sliding cylinders, under heavy loads. Journal of Basic Engineering. 87, 695-707.

[33] Dowson, D., Whitaker, A.V., 1968. A numerical procedure for the solution of the elastohydrodynamic problem of rolling and sliding contact lubricated by a Newtonian fluid. Proceedings of the Institution of Mechanical Engineers. 182, 119-134.

[34] Murch, L.E., Wilson, W.R.D., 1975. A thermal elastohydrodynamic inlet zone analysis. ASME Journal of Lubrication Technology. 97, 212-216.

[35] Ghosh, M.K., Hamrock, B.J., 1985. Thermal elastohydrodynamic lubrication of line contacts. ASLE Transaction. 28, 159-171.

[36] Sadeghi, F., Sui, P.C., 1990. Thermal elastohydrodynamic lubrication of rolling/sliding contacts. ASME Journal of Tribology. 112, 189-195.

[37] Houpert, L.G., Hamrock, B.J., 1986. Fast approach for calculating film thickness and pressures in elastohydrodynamically lubricated contacts at high load. Journal of Tribology. 108, 411-420.

[38] Yang, P.R., Wen, S.H., 1992. The behavior of non-Newtonian thermal EHL film in line contacts as dynamic loads. ASME, Journal of Tribology. 114, 81-85.

[39] Wolff, R., Nonaka, T., Kubo, A., et al., 1992. Thermal elastohydrodynamic lubrication of rolling/sliding line contacts. ASME Journal of Tribology. 114, 706-713.

[40] Wolff, R., Kubo, A., 1994. The application of Newton-Raphson method to thermal elastohydrodynamic lubrication of line contacts. ASME Journal of Tribology. 116, 733-740.

[41] Hsiao, H.S., Hamrock, B.J., 1994. Non-Newtonian and thermal effects on film generation and traction reduction in EHL line contacts conjunction. ASME Journal of Tribology. 116(4), 794-823.

[42] Yang, P., Wang, T., Kaneta, M., 1994. Thermal and non-Newtonian numerical analysis for starred EHL line contact. ASME Journal of Tribology. 128(2), 282-298.

[43] Salehizadeh, H., Saka, N., 1991. Thermal non-Newtonian elastohydrodynamic lubrication of rolling line contacts. ASME, Journal of Tribology. 113, 481-491.

[44] Liu, Z., Picken, D., He, T., et al., 2018. A thermal EHL model for connected rollers and its application on open seal-Houling interface. Journal of Tribology. 30, 1-34.

[45] Briggs, W.L., Henson, V.E., McCormick, S.F., 2000. A multigrid tutorial, second edition. SIAM: Philadelphia.

[46] Roelands, C.J.A., 1966. Correlation aspects of viscosity-temperature-pressure relationship of lubricating oils [PhD thesis]. Netherlands: Delft University of Technology.

[47] Wang, S.H., Zhang, H.H., 1987. Combined effects of thermal and non-Newtonian character of lubricant on pressure, film profile, temperature rise and shear stress in EHL. Journal of Tribology. 109, 666-670.

[48] Carslaw, H., Jaeger, J.C., 1959. Conduction of heat in solids. Oxford University Press: Oxford.

[49] Bisset, E.J., Glander, D.W., 1998. A highly accurate approach that resolves the u6pressure spike of EHL. Transaction, ASME, Journal of Tribolog. 110, 241-246.

[50] Venner, C.H., Ten Napel, W.E., 1989. Numerical calculation of the pressure spike in EHL. Lubrication Science. 2, 321-334.

BILINGUAL PUBLISHING GROUP
Pioneer of Global Academics Since 1984

Journal of Mechanical Materials and Mechanics Research
https://journals.bilpubgroup.com/index.php/jmmmr

ARTICLE

The Correlation of Gyroscope Axial Velocities

Ryspek Usubamatov

Kyrgyz State Technical University named after I.Razzakov, Bishkek, 720044, Kyrgyz Republic

ABSTRACT

In engineering, all movable expanse revolving objects manifest gyroscopic effects. These effects are created by the action of the outer load on the revolving items whose rotating mass originates eight inertial torques about two axes. Two torques of centrifugal forces, one torque of the Coriolis force originated by the rotating distributed mass, and the torque of the change in the angular momentum of the center mass act about each axis. The inertial torques activate rotations of the gyroscope by the determined correlation. Inertial torques depend on their geometry and orientation at the spatial coordinate system. The known analytical model for the rotation of the revolving disc about axes contains a mechanical error. This error was obtained by the incorrect integration of the centrifugal inertial torque. The corrected inertial torque yields the accurate expression for the interacted rotations of the revolving disc about axes.

Keywords: Gyroscope theory; Inertial torque; Correlation of angular velocities

1. Introduction

Physicists and mathematicians started studying the gyroscopic effects of the revolving disc, beginning from the time of intensive applications of engineering discoveries for human economics. They developed only one part of the mathematical model which is the inertial torque presented by the change in the angular momentum (L. Euler). The physics of other gyroscopic effects were explained intuitively as the operation of the inertial torques that are unacceptable for the analytical modelling of their processes [1-4]. The analytical formulation of the gyroscopic effects remained unsolved until our time [5-8].

The studies of gyroscopic effects show their foundation is based on several principles of classical mechanics that were developed over three centuries [5-8]. One of the physical principles of gyroscopic effects is the mechanical energy conservation law was for-

*CORRESPONDING AUTHOR:
Ryspek Usubamatov, Kyrgyz State Technical University named after I.Razzakov, Bishkek, 720044, Kyrgyz Republic; Email: ryspek0701@yahoo.com

ARTICLE INFO
Received: 27 February 2023 | Revised: 3 March 2023 | Accepted: 14 March 2023 | Published Online: 24 March 2023
DOI: https://doi.org/10.30564/jmmmr.v6i1.5509

CITATION
Usubamatov, R., 2023. The Correlation of Gyroscope Axial Velocities. Journal of Mechanical Materials and Mechanics Research. 6(1): 36-40. DOI: https://doi.org/10.30564/jmmmr.v6i1.5509

mulated at the beginning of the 20 century. Over the last hundred years, researchers had the time and opportunities to derive mathematical models for the gyroscope theory but did not do it [9-13]. Gyroscopic effects were resolved finally in our time and published in several manuscripts and one book.

The gyroscope theory shows sophisticated rotations of the revolving disc based on several principles of physics mechanics. These principles are the centrifugal, and Coriolis forces, the change in the angular momentum, and kinetic energy conservation which were developed over three hundred years. The gyroscopic effects are the manifestation of the operation of principles pointed out above that is presented by the action of the sets of inertial torques and correlated rotations of the revolving disc [14]. One set presents four inertial torques operating about one axis, which are generated by two centrifugal and one Coriolis force, and the torque of the change in the angular momentum. One torque of centrifugal force act on two axes and the other torques act on one axis. The expressions of the gyroscopic inertial torques and their operations are shown in **Table 1** [15,16].

Table 1. Inertial torques operating on the revolving disc with the angle $\gamma = 0$.

Inertial torques generated by	**Operation**	**Expression**
Centrifugal forces	Opposition	$T_{ct.i} = (4\pi^2 / 9) J\omega\omega_i$
	Precession	
Coriolis forces	Opposition	$T_{cr.i} = (8 / 9) J\omega\omega_i$
Change in angular momentum	Precession	$T_{am.i} = J\omega\omega_i$

Table 1 contains expressions ω and ω_i which are the velocity of the revolving disc about axis *oz* and *i*, accordingly; *J* is the moment of inertia of the revolving disc. The operation of the inertial torques and rotations of the revolving disc about axes of the spatial coordinates system are shown in **Figure 1** [16].

Figure 1 contains the following expressions: *T*, $T_{ct.i}$, $T_{cr.i}$, $T_{am.i}$ are the external, centrifugal, Coriolis torque, and the torque of the change in the angular momentum, accordingly, γ is the angle of the revolving disc tilt, and other components are as specified above.

The mechanical energy conservation law for revolving items maintains the equality of the potential and kinetic energies about axes of rotation [16]. This canon enables defining the dependency for the correlated action of the inertial torques of the revolving disc and its rotations about two axes. The known analytical model for the correlation of the revolving disc rotations around axes contains errors [15]. The presented manuscript shows the origin of the incorrect solution of the correlation of the angular velocities for the revolving disc about axes of rotation.

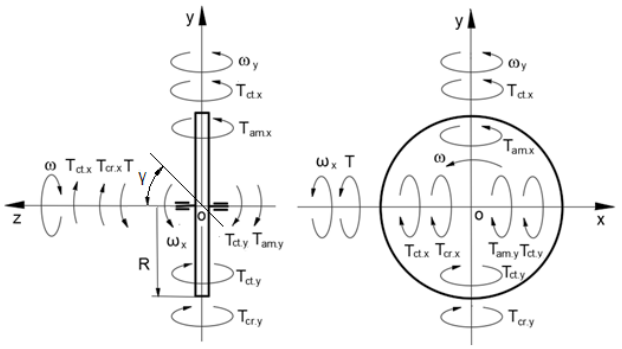

Figure 1. Outer and inertial torques operating on the revolving disc and its rotations.

2. Methodology

The mechanical energy of the body remains constant in any of its locations in the expanse by the mechanical energy conservation law. The gyroscopic effects express the operation of inertial torques of the revolving disc that contains the kinetic energies of their axial rotations. These energies are equal and express the canon of the mechanical energy conservation law [15]. The expressions of inertial torques operating on the revolving disc of the inclined axis on the angle γ reflect its kinetic energies about axes which are shown below and in **Figure 1**:

$$-T_{ct.x} - T_{cr.x} - T_{ct.y} - T_{am.y} = T_{ct.x}\cos\gamma + T_{am.x}\cos\gamma - T_{ct.y} - T_{cr.y} \quad (1)$$

where the expression of the torques is as specified in **Table 1** and **Figure 1**.

Equation (1) expresses torques operating about axes in the spatial coordinate system and differs from similar ones in publications [15]. The method of the causal investigatory correlation enables defining of the looped operation of the inertial torques. The revolving disc tilts on the angle γ in the counter

clockwise direction by the operation of the outer torque T. The external torque T activates the inertial opposition torque $T_{r.x} = T_{ct.x} + T_{cr.x}$ of the centrifugal and Coriolis forces of the left side of Equation (1) originating from the rotating mass of the revolving disc. The opposition torque T_{rx} of axis *ox* originates the precession torques T_{px} of the centrifugal force and the change in the angular momentum of axis *oy*. The torques T_{px} of the right side of Equation (1) is multiplied by cosγ, $T_{p.x} = T_{ct.x}\cos\gamma + T_{am.x}\cos\gamma$ which originates the opposition torques $T_{ct.y}$ and $T_{cr.y}$ of the centrifugal and Coriolis forces without cosγ. The opposition torques $T_{ct.y}$ and $T_{cr.y}$ are produced by the torque $T_{p.x}$ operating on axis *oy.* The resulting torque $T_{res.y} = T_{ct.x}\cos\gamma + T_{am.x}\cos\gamma - T_{ct.y} - T_{cr.y}$ of the right side of Equation (1) operating on axis *oy* originates the precession torque $T_{p.y} = T_{ct.y} + T_{am.y}$ of the centrifugal force and the change in the angular momentum of axis *ox*. The torques $T_{p.y}$ is combined with the opposition torque $T_{rx} = T_{ct.x} + T_{cr.x}$. Then the resulting torque of axis *ox* is presented by the expression $T_{res.x} = T_{ct.x} + T_{am.x} + T_{ct.y} + T_{cr.y}$, which formulates with the external torque T, the opposition torque $T_{r.x}$, and precession torques $T_{r.x}$ of axes *ox* and *oy*, accordingly. The looped system of the inertial torques of the revolving item shows the equality of its kinetic energies of axis *ox* and *oy*. The expressions of the inertial torques of each axis contain the velocities ω_x and ω_y of two axes *ox* and *oy* that demonstrate their correlations. The expressions of the inertial torques (**Table 1**) are substituted into Equation (1) that yields:

$$-\frac{4\pi^2}{9}J\omega\omega_x - \frac{8}{9}J\omega\omega_x - \frac{4\pi^2}{9}J\omega\omega_y - J\omega\omega_y = \frac{4\pi^2}{9}J\omega\omega_x\cos\gamma + J\omega\omega_x\cos\gamma - \frac{4\pi^2}{9}J\omega\omega_y - \frac{8}{9}J\omega\omega_y \quad (2)$$

Simplification of Equation (2) yields:

$$\omega_\gamma = -[4\pi^2 + 8 + (4\pi^2 + 9)\cos\gamma]\omega_x \quad (3)$$

where the sign (-) is removed because shows the direction of the inertial torque and does not relate to the rotations of the revolving disc.

Equation (3) is the correlation of the velocities for the revolving disc as a function of the angle γ of the inclined disposition about axis *ox*. For the angle $\gamma = 0$, Equation (3) is $\omega_y = (8\pi^2 + 17)\omega_x$. The correlation of the disc velocities ω_y/ω_x of two axes by Equation (3) is shown in **Figure 2**.

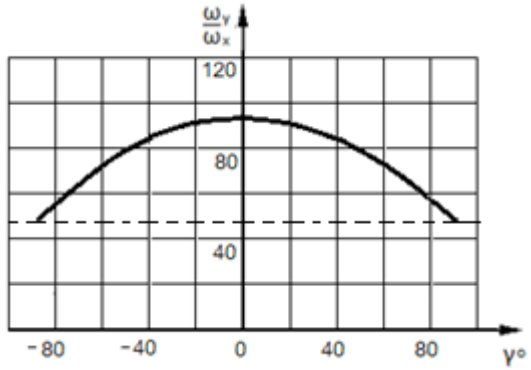

Figure 2. The correlation of the disc axial velocities ω_y/ω_x as a function of the angle γ.

Equation (3) does not maintain when the revolving disc axis has a vertical disposition ($\gamma = \pm 90^o$) that gives $\omega_y = 0$ because inertial precession torques act about axis *oy*. The small tilt of the revolving disc of horizontal disposition on axis *ox* yields the turn on 90^o about axis *oy*. The expression $\varphi = -(8\pi^2 + 17)\gamma$ yields $\gamma = 0.938^o = 58'22''$. This correlation is validated in the rotations of the gyroscopic frames that call gimbals. The small swing of the gyroscope's outer frame on $\gamma = 0.938^o$ yields the high rotation on $\varphi = 90^o$ of the inner frame which measurement is problematic on the movable parts. The laboratory gyroscope can validate the rotation of the inner frames from $\varphi = -90^o$ to $\varphi = 90^o$ and the rotation on the angle $\gamma = 1{,}876^o = 1^o52'33''$ of the outer frames. The rotations of the gyroscope frames confirm the correctness of Equations (2) and (3).

Figure 3 shows the change in the angular dispositions of the inner and the outer gyroscope frames. The theoretical and practical tests discover the nature of gyroscopic frame rotations that were one in the series of former unsolved gyroscopic effects.

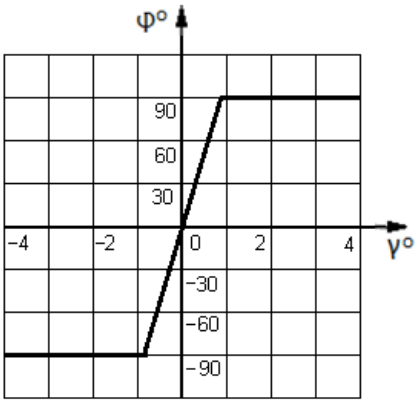

Figure 3. The turn of the outer frame to γ versus the inner one on φ for the revolving disc.

3. Results and discussion

The first publications related to gyroscopic effects contain unpleasant mistakes of the pioneering work for complex problems. The mistakes are presented by the incorrect mathematical processing of a complex integral equation for the inertial torque originated by the centrifugal forces of the rotating mass of the revolving disc [14]. This mathematical mistake yielded the incorrect solution for the correlation of gyroscope axial rotations. The exact expression for inertial centrifugal torque gives the twice value for the published incorrect expression. The exact centrifugal torque decreases twice the velocity of the gyroscope about axis *ox* and increases twice the velocity about axis *oy*. The recorded tests of the gyroscope rotation about axis *oy* give the same result as for the test with the incorrect expression of the centrifugal torque. The gyroscope angular velocity about axis *ox* did not measure because of the too-small turn which was problematic technically for the movable parts. The correction of the theory of gyroscopic effects enables avoiding criticism from readers.

4. Conclusions

The breakthrough theory of gyroscopic effects for revolving items can solve all problems for gyroscopic devices. This theory yields a new chapter in the mechanics of dynamics for rotating bodies and closes one gap in science. Engineering science received a new method for an analysis of the inertial torques originated by the rotating items and computing dynamical parameters of gyroscopic effects. The first publications of the theory of gyroscopic effects contain the incorrect expressions for the centrifugal torque and the related correlations. The corrected expressions will be positively used in practice and educational processes.

Conflict of Interest

There is no conflict of interest.

References

[1] Cordeiro, F.J.B., 2015. The Gyroscope [Internet]. Createspace: NV, USA. Available from: https://www.google.kg/books/edition/The_Gyroscope/P31ZvwEACAAJ?hl=en

[2] Greenhill, G., 2015. Report on gyroscopic theory. Relink Books, Fallbrook: CA, USA.

[3] Scarborough, J.B., 2014. The gyroscope theory and applications. Nabu Press: London.

[4] Weinberg, H., 2011. Gyro Mechanical Performance: The Most Important Parameter [Internet]. Available from: https://www.analog.com/en/technical-articles/gyro-mechanical-performance.html

[5] Hibbeler, R.C., Yap, K.B., 2013. Mechanics for engineers-statics and dynamics, 13th edition. Prentice Hall, Pearson: Singapore.

[6] Gregory, D.R., 2006. Classical mechanics. Cambridge University Press: New York.

[7] Taylor, J.R., 2005. Classical mechanics. University Science Books: California, USA.

[8] Aardema, M.D., 2005. Analytical dynamics: Theory and application. Academic/Plenum Publishers: New York.

[9] Liang, W.C., Lee, S.C., 2013. Vorticity, gyroscopic precession, and spin-curvature force. Physical Review D. 87, 044024.

[10] LeMoyne, R., Mastroianni, T., McCandless, C., 2018. Implementation of a smartphone as a wearable and wireless accelerometer and gyroscope platform for ascertaining deep brain

stimulation treatment efficacy of parkinson's disease through machine learning classification. Advances in Parkinson's Disease. 7, 19-30. DOI: https://doi.org/10.4236/apd.2018.72003

[11] Yong, C.Y., Sudirman, R., Mahmood, N.H., et al., 2013. Motion classification using proposed principle component analysis hybrid k-means clustering. Engineering. 5(5B), 25-30. DOI: https://doi.org/10.4236/eng.2013.55B006

[12] Crassidis, J.L., Markley, F.L., 2016. Three-axis attitude estimation using rate-integrating gyroscopes. Journal of Guidance, Control, and Dynamics. 39, 1513-1526.

[13] Nanamori, Y., Takahashi, M., 2015. An integrated steering law considering biased loads and singularity for control moment gyroscopes. AIAA guidance, navigation, and control conference 2015, MGNC 2015—Held at the AIAA SciTech Forum 2015. American Institute of Aeronautics and Astronautics Inc.: USA.

[14] Usubamatov, R., Allen, D., 2022. Corrected inertial torques of gyroscopic effects, Hindawi. Advances in Mathematical Physics. 1-7. DOI: https://doi.org/10.1155/2022/3479736

[15] Usubamatov, R. (editor), 2015. Mathematical model for gyroscope's Gimbal motions. 4th International Conference on Advances in Engineering Sciences & Applied Mathematics (ICAESAM'2015); 2015 Dec 08-09; Kuala Lumpur (Malaysia). p. 41-44.

[16] Usubamatov, R., 2022. Theory of gyroscope effects for rotating objects. Springer, Cham: Switzerland.

BILINGUAL PUBLISHING GROUP
Pioneer of Global Academics Since 1984

Journal of Mechanical Materials and Mechanics Research
https://journals.bilpubgroup.com/index.php/jmmmr

ARTICLE

Smart Elevator Systems

Kheir Al-Kodmany

Department of Urban Planning and Policy, the University of Illinois at Chicago, Illinois, 60607, Chicago

ABSTRACT

Effective vertical mobility is a crucial element in the design and construction of tall buildings. This paper reviews recent "smart" developments in elevator technologies and analyzes how they affect the construction and operation of tall buildings. In an approachable and non-technical discourse, it maps out, arranges, and compiles complicated and dispersed information on various elements of elevator design. It discusses hardware-based innovations, such as AC and gearless motors, machine-room-less (MRL) elevators, regenerative drives, elevator ropes, and LED lighting, as well as software-based solutions, such as destination dispatching systems, people flow solutions, standby mode, and predictive maintenance applications. Future vertical transportation models are also discussed, including multi-directional elevators and circulating multi-car elevators. Lastly, the paper suggests fruitful avenues for further studies on the subject, such as robotics, 3D printing, and the impact of the COVID-19 pandemic on elevator design.

Keywords: Energy efficiency; Energy conservation; Long distances; Hardware; Software; Applications

1. introduction

1.1 Overview

Cities all over are expanding vertically. The main forces behind building upward are population expansion (driven by natural population growth and major rural-to-urban migration), rapid urban regeneration, soaring land costs, active agglomeration, and globalization. Project owners have even purchased excess development rights from surrounding structures to build a taller structure. Some builders, building owners, and tenants may have personalities that push them to build taller than their competitors or have their condo or business address in a supertall structure. Many consider cities with skylines comprised of tall structures to be progressive and suc-

*CORRESPONDING AUTHOR:
Kheir Al-Kodmany, Department of Urban Planning and Policy, the University of Illinois at Chicago, Illinois, 60607, Chicago; Email: kheir@uic.edu

ARTICLE INFO
Received: 27 February 2023 | Revised: 8 March 2023 | Accepted: 14 March 2023 | Published Online: 24 March 2023
DOI: https://doi.org/10.30564/jmmmr.v6i1.5503

CITATION
Al-Kodmany, K., 2023. Smart Elevator Systems. Journal of Mechanical Materials and Mechanics Research. 6(1): 41-53. DOI: https://doi.org/10.30564/jmmmr.v6i1.5503

cessful. Moreover, tall buildings have shown to be magnets for new growth, attracting additional firms and boosting the local economy. After completion, several tall buildings find up in the portfolios of investment and insurance companies, giving economic rewards for more than just the developer.

At any rate, according to the United Nations, 70% of the world's 9.7 billion people will live in cities by 2050, up from 51% in 2010 [1,2]. To accommodate our expanding population, buildings are multiplying and rising higher. Thus, we need to start considering the most effective strategies to reduce consumption and the urban energy footprint. Buildings use 40% of the energy in the world; and therefore, they should be given priority in cities' efforts to minimize their carbon footprints as the fight against climate change gains steam [2,3].

As tall buildings proliferate in cities and test the limits of height, elevator design faces new challenges. Architects, engineers, and developers prioritize elevators throughout the phases of building design. The building's core, or "the backbone of a tall building", is made up of the elevator and stairs. This core determines the construction of the building and the floor layouts of the surrounding units. Simultaneously, engineers are working diligently to reduce the required space and energy to operate elevators, decrease the environmental impact, while improving safety, and comfort [2,4].

1.2 Goals and objectives

In tall or supertall buildings, any improvement in elevator design and manufacturing will have far-reaching effects on the costs, user comfort, and the environment. This paper traces recent developments in the elevator industry with the purpose of educating masses of architects and engineers. It delves into the "smart" evolution of elevator technology and examines its implications for the building and maintenance of skyscrapers. It organizes and gathers complex and dispersed knowledge on numerous areas of elevator design in a comprehensible and non-technical manner. Recent technological breakthroughs are put into perspective by analyzing their implementation in large-scale undertakings. The concept of "smart" is increasingly being used as a benchmark for modern engineering. Therefore, the discussion gives helpful information for choosing "smart" decisions when it comes to including elevators in high-rise buildings. Overall, the paper intends to provide an educational coverage of smart technologies, energy-efficient, space -saving elevator systems, and new elevators that generate "clean energy".

2. Energy-efficient hardware

2.1 DC and AC motors

The switch from traditional brushed DC (direct current) motors to more efficient AC (alternating current) motors is one of the most significant advancements in elevator technology. Before the 1990s, elevator systems relied on DC motors because it was easier to control elevator acceleration, deceleration, and stopping with this form of power. AC power was usually only used in freight elevators, where speed and comfort are less critical than in passenger elevators. By the late 1990s, however, more elevators had moved to AC machines because motor controller technology had advanced enough to regulate AC power, enabling smooth stopping, acceleration, and deceleration. DC motors were great when they first came out. Still, newer AC gearless motors are better in terms of performance, energy efficiency, and the ability to send extra power back into the building's electrical system [4-6].

2.2 Geared and gearless motors

Elevators in high-rise buildings are primarily traction elevators, which can either be geared or gearless. Because they lack gears, gearless elevator motors can be up to fifty percent more compact than their geared counterparts. As a result of the engine being scaled down, all of the other components will likewise be reduced in size. In machines that use gears, the electric traction motor rotates a reduction gearbox, and the gearbox's output rotates

a sheave that serves as a passageway for the rope that connects the car to the counterweights. Gearless elevators, on the other hand, do not have a gear train since the drive sheave is instead directly connected to the motor. This eliminates the requirement for a gear train as well as the energy losses that come along with it. Therefore, one of the primary benefits of gearless motors is that they are approximately 25 percent more efficient than geared motors. Because of their higher torque and lower revolutions per minute (RPM), gearless engines are able to run more quickly and have a longer lifespan than their conventional counterparts. The cost of gearless elevators, including the cost of materials, installation, and maintenance, is often higher than that of geared elevators. This is the most significant disadvantage of gearless elevators. AC gearless motor machines are used in more elevators today despite that they are more expensive. This is because they have higher overall efficiency and may be utilized for a greater amount of time [5,7,8].

2.3 Machine-Room-Less (MRL) technology

Elevator equipment used to be so big that it needed its own room, usually placed above the hoistway on the roof of a building and at least 8 feet tall. The machine room was costly because it was needed to support heavy machinery. Introduced in the mid-1990s, MRL technology was one of the enormous advances in elevator design since elevators became electric a century before. Elevators without a machine room employ a gearless traction machine positioned in the hoistway. Utilizing a counterweight aids the machine in spinning the elevator sheave, which propels the cab through the hoistway. As a result, manufacturers reconfigured the motors and any other equipment that would normally be placed in a machine room to fit inside the hoistway, which eradicated the need to construct a machine room (**Figure 1**). The reduced starting current needed for the MRL also contributes to its energy efficiency. The MRL uses only 30 to 40 percent of the energy used by comparable traction and hydraulic motors. The MRL is a high-performance, space-saving, and energy-efficient elevator as a result [6,9]. It becomes even more energy-efficient if it is combined with regenerative drives (see next section). Today, MRL elevators are increasingly common.

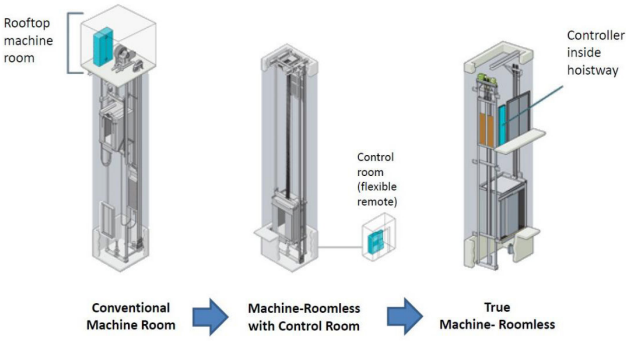

Figure 1. Gearless machine-roomless revolution.

Source: Adapted from otisworldwide.com.

2.4 Regenerative drives

Another significant development in energy-efficient elevator technology is the use of regenerative drives, which allow energy to be recycled rather than wasted as heat. They function by accumulating and transforming the energy expended during braking to keep the elevator's speed constant. In order to balance the weight of the elevator vehicle and the passengers, traction elevators employ a counterweight. The counterweight is optimally sized, roughly equivalent to a car loaded at 40%-50% of capacity. The elevator will perhaps overtax the motor and brake system if the counterweight is too heavy or too light. Instead, a midway weight works well to balance energy consumption in both upward and downward motions. The elevator uses brakes to maintain its rated speed when the elevator car is loaded less than or more than 50% of its maximum capacity (cars moving up are light or heavy, respectively). When applying breaks, the AC motor functions as an energy generator by converting mechanical "heat" energy into electrical energy and channeling it back into the facility's electrical grid [7,10]. Further, because there is no longer a requirement to cool equipment that is subjected to the excessive heat generated by traditional motors, this results in an extra reduction in the

amount of energy consumed (**Figure 2**). The length of travel, frequency, pattern of use, and device age affect energy savings. Longer distances and more trips generate more energy [11,12] (**Figure 3**).

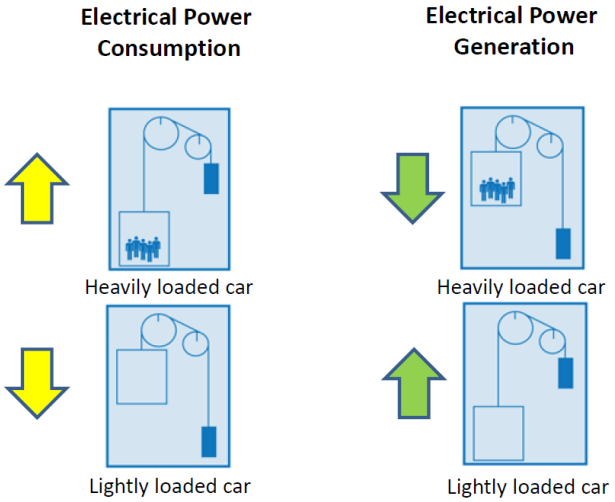

Figure 2. The regenerative drive system.

Source: Adapted from otisworldwide.com.

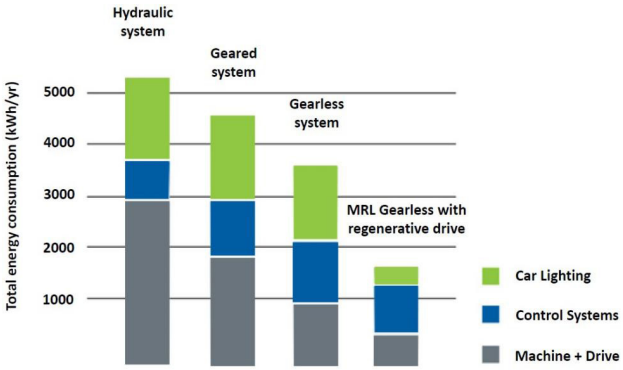

Figure 3. A comparison of energy consumption among different elevator systems.

Source: Adapted from otisworldwide.com.

2.5 Elevator rope

Because it links the elevator engine with the cab, sheaves, and counterweight, the elevator rope is a crucial part of traction elevators. Steel ropes hold cabins. However, in very tall buildings, the rope gets too long and too heavy to the point that it cannot support its own weight. As height increases, starting currents and energy usage rise, increasing energy consumption. In other words, the combined weight of the steel ropes required to operate elevators to supertall heights is the largest obstacle. Each elevator requires four to eight ropes, and at a certain height, it becomes impractical to utilize them for single runs on supertall structures, forcing builders to incorporate one or more transfer levels, or "sky lobbies". In response to this challenge, elevator manufacturers have been strengthening cables. The Schindler's aramid fiber rope is more robust and lighter than the steel one. Otis' tiny Gen2 elevators use ultra-thin wires encased in polyurethane instead of steel ropes. Mitsubishi produced a more potent, denser string with concentric steel wire (**Figure 4**). These more robust, lighter cords move elevator cabs more efficiently, conserving energy [11,13,14].

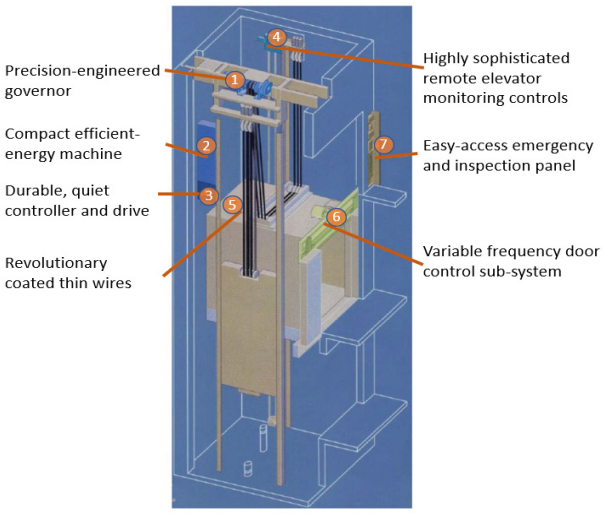

Figure 4. Diagram of OTIS GeN2 lift.

Source: Adapted from otisworldwide.com.

The KONE "UltraRope" is the most significant breakthrough. It has a carbon fiber core and a unique high-friction coating, allowing cars to travel up to 1,000 m (3,280 ft). This is twice the current 500 m (1,640 ft) limit. A 1000-m UltraRope weighs 10% of steel ropes. The 90% reduction in rope mass saves considerable energy. The 1-kilometer, 3,281-foot-tall Jeddah Tower in Saudi Arabia (construction on hold) plans to install the super-light KONE UltraRope elevators, reducing the number of required sky lobbies. Using UltraRope, an elevator can travel the 653 me-

ters from the Jeddah Tower's base to the observation deck in just one trip. In South Quay Plaza, one of the highest residential buildings in Europe and the first to be outfitted with KONE UltraRope, eight of these elevators were built [13]. In the future, technology such as UltraRope will enable elevators to ascend higher and reduce the need for sky lobbies. During the next iteration, KONE plans to devise methods for moving people that high and quickly while ensuring their safety and well-being particularly related to variations in pressure and temperature at high altitudes.

2.6 Double-deck elevators

A double-deck elevator consists of two stacked cabs where one serves floors with even numbers, and the other serves floors with odd numbers. As skyscrapers get higher, reducing the number of shafts needed becomes more important because they eat up valuable interior space on every floor (**Figure 5**). Double-deck elevators are most useful for applications in very tall buildings, particularly for shuttle services [14,15]. However, the double-deck elevators suffer from some operational challenges. Equal floor rise could present a limitation; i.e., for local service, double-deck elevators must load and unload two decks simultaneously. Even though traffic is reduced during off-peak hours, both decks will be operating [15,16].

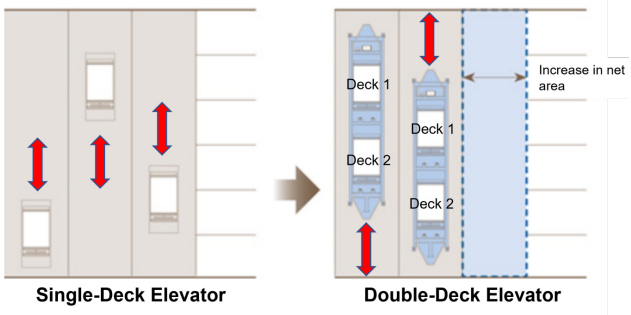

Figure 5. Double-deck elevators save on the number of shafts needed to serve a building.

Source: Adapted from hyundaielevator.com.

2.7 The TWIN systems

Sharing similar characteristics with double deck systems, TWIN is an elevator system in which two standard cabs are installed within the same shaft but operate independently. A device that monitors the distance between two elevators prevents them from collisions (**Figure 6**). A computerized system optimizes travel for both cabins by assigning passengers to cabs most efficiently, reducing wait time and empty journeys, and saving energy [16-18]. Simply, the system enables more elevators with fewer shafts – it is estimated to require one-third fewer shafts than conventional elevators, saving core space. In addition to freeing up valuable space, the TWIN system reduces the required building materials for shafts, decreasing embodied energy. Because there is just one control machine for both elevators in the same shaft, significant space and energy are saved as a result of this design decision [17,19].

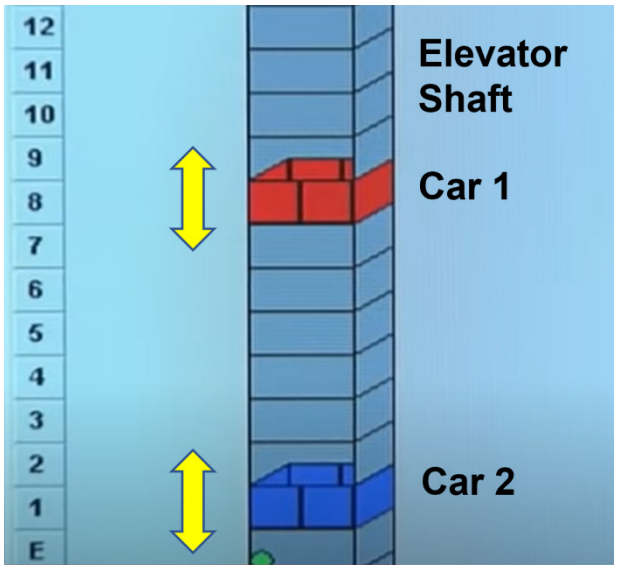

Figure 6. In the TWIN system, each shaft holds two cars that operate independently. A computerized system and sensors coordinate their movements and ensure no collisions.

Source: Adapted from youtube.com/watch?v=DMfqwhj_S3U.

2.8 LED lighting

Energy-efficient light-emitting diode (LED) cab lights within an elevator car and their adjustment to motion detectors are among the most critical factors in a building's efficient power consumption. LEDs are significantly more energy efficient than incandes-

cent, halogen, and fluorescent light bulbs. LEDs emit less heat, which reduces the energy required to cool the cab. Numerous new structures currently incorporate LED lighting. Often, building owners are replacing conventional elevator lighting systems with LED illumination [12,20,21].

2.9 Computerized roller guides

Moving an elevator quickly and over great distances requires more than just strong motors and current. Fast-moving elevators, like bullet trains, need exceptionally smooth rails and rail joints to travel quickly. Any skyscraper will undoubtedly need a lot of rail joints because the vertical arrangement of elevator rails restricts their length to roughly 4.9 m (16 ft) due to alignment precision constraints. Elevators must also consider minute variations in the spacing between guide rails that result from temperature changes (contraction and expansion), wind forces, and other factors that cause skyscrapers to sway slightly during the day and night [22-24]. In response to these problems, ThyssenKrupp created automated roller guides. These guides exert forces in the opposite direction from the guide rails' normal direction of travel, reducing the effects of the bumps. While the elevator car ascends and falls, roller guides maintain contact between the rollers and the guide rails. They are also managed by a mechanism that pushes and pulls against the rails to avoid any misalignments or imperfections from generating tremors and rattle. These active roller guide systems serve this purpose as clever real-time shock absorbers. They mimic how a motorist may act if they knew of a sizable pothole in the road and swerved a little to avoid it. When a pothole is on the right side of the road, the driver will turn slightly to the left, and vice versa [22,25] (**Figure 7**).

2.10 Braking system

Mitsubishi developed a new braking system to ensure safety at higher speeds and longer distances. Safety mechanisms will immediately engage the brakes if "cables become transected", grabbing the guide rails. A revolutionary two-tier braking system that employs ceramic brake shoes can withstand shocks and extreme heat over 1,000 degrees Celsius (1,800 degrees Fahrenheit). Hence, a disc brake stops the primary pulley system in regular operation. In the event that the system detects a train going at an unsafe rate of speed, it will activate a mechanism at the train's undercarriage to grab the rails and bring the train to a stop within 15 meters (50 ft) [26-28].

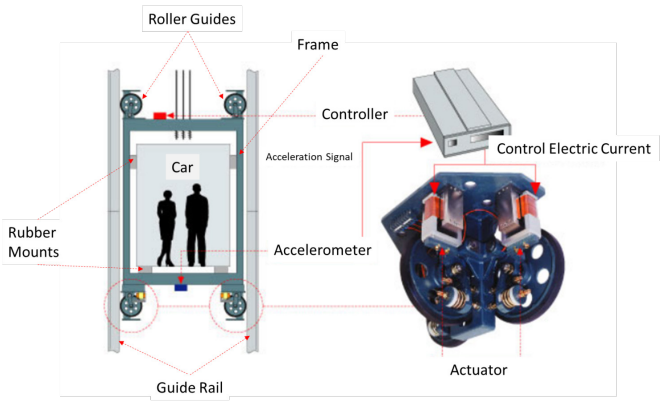

Figure 7. Illustration of the computerized roller guides system.

Source: Adapted from mitsubishielectric.com/.

2.11 Air pressure differential

When designing and constructing high-speed elevator systems that travel great distances, such as in supertall and megatall skyscrapers, the air pressure differential is a consideration. The first difficulty with air pressure is related to the elevators' rapid passage between floors, which causes air resistance in the elevator shaft. The air-pressure effect is comparable to that of a subway: as a train pulls into the station, it pushes a wall of air ahead of it. Similarly, when a standard 4,500-kilogram car with a 7,300-kilogram counterweight ascends or descends rapidly in an elevator shaft, it causes a tremendous amount of air displacement. With a high-pressure zone above the car and a low-pressure zone below it, the hoistway doors above the car are forced into the hallway, while the hoistway doors below the car are sucked into the hoistway. As a solution, ThyssenKrupp affixed wedge-shaped aluminum shrouds to the top and bottom of the cabs to make them more

aerodynamic as they ascend and descend the shafts. The cab's resulting aerodynamic shape reduces air resistance, minimizes air displacement, diminishes door rattling, and lessens wind noise [22,23].

The second air-pressure problem is connected to the safety and comfort of the passengers, especially concerning the "ear-popping" effect when the elevator goes at a higher speed. This problem is more noticeable in the descending sequence, but it occurs because of the rapid and abrupt shift in air pressure that happens as the elevator ascends and falls. It's vital to remember that elevators in super and megatall buildings descend faster than a descending commercial flight. An airplane's landing procedure may take around 30 minutes, giving plenty of time to regulate the air pressure within the aircraft. In contrast, the amount of time elevators have to change the air pressure or depressurize might be as short as 30 seconds. This limits the time passengers in elevators have to adjust. In response, ThyssenKrupp developed a strategy that involves pressurizing vehicles (adding extra air pressure within the cars to make up for pressure drops) and then gradually releasing it to prevent passengers' ears from popping. Nonetheless, in all instances, because of the air-pressure issue, elevators continue to descend at a maximum rate of 10 m per second (33 ft/s) [22,23,29].

3. Energy-efficient software

Studies of elevator traffic have revealed that the elevator's cycle significantly impacts energy consumption. The operation of an elevator, the number of levels visited, peak load, low load, and empty trips may all be analyzed to develop energy consumption models. These models help to formulate practical management suggestions and control tactics. New software is empowering this endeavor [13,30].

3.1 Destination dispatching systems

Elevators answer calls when users press the up and down buttons. This technique works fine in buildings with limited "vertical ridership" and does not experience "rush hour" traffic. In heavy traffic, many buttons are pressed, causing elevator stops and longer travel times. Each stop in a high-speed elevator at six m/s may take 10-13 s. Elevator designers created the destination dispatching system (DDS) to address this problem. It was initially developed in the 1990s following the boom in more excellent microprocessor capability throughout the 1980s. A DDS is an optimization strategy for multi-elevator systems, which puts passengers for the same destinations into the same elevators. The technology analyzes passengers' data in real-time and efficiently groups destinations, reducing elevator stops. When entering a destination using keypads or touch screens on the Destination Operation Panel (DOP), which is often strategically located in the lobby, the system indicates and directs each passenger to the allotted elevator to board [14,31] (**Figure 8**).

3.2 People flow solutions

People Flow Solutions, much like the DDS, are intended to regulate demand on elevators and improve the flow of foot traffic, but primarily in more extreme circumstances. For example, KONE's Advanced People Flow Systems provide enhanced safety, convenience, and comfort. They integrate access and destination control, communication, and equipment monitoring to provide a seamless experience for users moving between facilities [18,32]. A solution that is both modular and linked, enabling tailored user experiences and touchless access that can be adapted to meet the specific requirements of a building.

3.3 Standby mode

Standby mode puts elevators in "hibernation" or "sleep" mode. At certain hours of the day, there isn't enough demand to warrant the use of all elevators—the majority of elevators operate between 20 and 30 percent of the time. Contrary to popular belief, elevators need power even when they are not in use. When cabs are idle, elevator systems must be kept powered, so they are prepared for the next passenger call. As such, the standby solution shuts down elevator machinery when not in use, conserving en-

ergy. When the car is vacant, the in-cab sensors and software put the elevator in a state known as "sleep mode", which turns off the lights, fans, music, and television screens. Depending on the control system, lighting style, floor displays, and operating consoles in each level and elevator cabin, the standby solution can save anywhere from 25% to 80% of the elevator's total energy consumption [19,33].

3.4 Predictive maintenance Apps

The creation of artificial intelligence- and machine learning-based algorithms have led to getting real-time updates on the status of an elevator. As such, new apps enable predictive maintenance. They empower building owners to use elevator data to diagnose, analyze, and notify them of maintenance needs and possibly automatically resolve service issues before they arise. With an IoT device connected to the elevator controller, the owner can gather precise information about the elevator's parts, identify flaws and weak signals before a failure, and offer repair assistance to specialists. Apps give building owners real-time insights from their phones or mobile devices to operate better and manage their buildings [20,34].

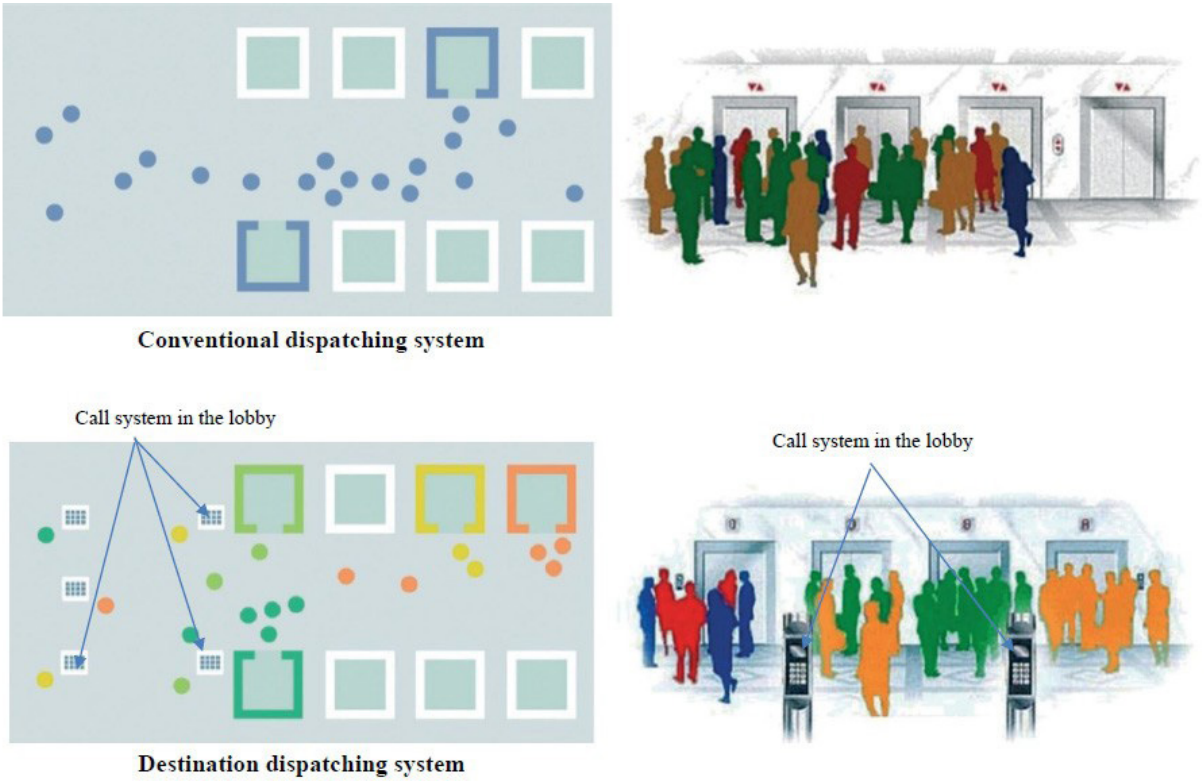

Figure 8. Conventional (top) versus destination dispatching system (bottom).

Source: Adapted from ThyssenKrupp.com.

4. Future developments

Since long before the concept of "smart" became popular, the elevator business has been actively seeking to improve elevator performance, including speed (**Table 1**), comfort, and those related to space and energy efficiency. The "positive-energy" elevator is the hoped-for culmination of the elevator industry's significant experience and ambition. Elevators that conserve energy and space, have motors that are not prohibitively expensive, are made of long-lasting materials, and have smart dispatching systems are still a primary focus of research. Solar elevators, in which solar panels are mounted on the hoistway to create power that may then be used to drive the elevator as well as contribute additional power to the city's power grid, are currently being developed by a few different firms.

Table 1. Skyscrapers with the fastest elevators (compiled by author).

Rank	Building	Speed in Seconds m/ft	Year of Completion	Building's Height m/ft	Elevator Supplier
1	CTF Finance Center, Guangzhou, China	20 (66)	2016	530 (1,739)	Hitachi
2	Shanghai Tower, Shanghai, China	18 (59)	2015	632 (2,074)	Mitsubishi
3	Taipei 101, Taipei, Taiwan	16.8 (55)	2004	509 (1,670)	Toshiba
4	Yokohama Landmark Tower, Yokohama, Japan	12.5 (41)	1993	296 (971)	Mitsubishi
5	One World Trade Center, New York City, U.S.A.	10.16 (33.33)	2014	541 (1,776)	Thyssenkrupp
6	Burj Khalifa, Dubai, U.A.E.	10 (33)	2010	828 (2,717)	Otis
7	Sunshine 60 Building, Tokyo, Japan	10 (33)	1978	240 (787)	Mitsubishi
8	Shanghai World Financial Center, Shanghai, China	10 (33)	2008	492 (1,614)	Thyssenkrupp
9	China World Trade Center Tower III, Beijing, China	10 (33)	2010	330 (1,083)	Schindler
10	John Hancock Center, Chicago, U.S.A.	9.1 (30)	1969	344 (1,129)	Otis

4.1 Net-zero solar energy elevator

Solar electricity is becoming increasingly popular, so an elevator that runs on solar energy could be a plausible solution to save energy. A net-zero elevator system produces at least as much energy as it consumes over a year. German elevator manufacturer ThyssenKrupp is working on a net-zero solar energy elevator prototype called the Synergy Elevator. It incorporates state-of-the-art energy-saving features, including a regenerative drive and LED cab lighting, a more efficient controller capable of a deep-sleep standby mode, and an auto-power-down feature that shuts off the cab lights and fan when the elevator is not in use. These features reduce the total standby power draw by about 75%. The prototype integrates a rooftop solar photovoltaic (PV) array to offset the elevator's energy consumption. The 3.75 kW solar PV system was designed to produce about 4,000 kWh per year in a climate similar to that of Boston—this prototype was tested in USA CSE's Boston Headquarters [35,36].

Similarly, Schindler Elevator Corp. introduced a solar-powered elevator prototype. The Schindler Solar Elevator uses rooftop solar panels and a Hybrid Energy Manager (HEM) to store solar energy in batteries to power up to 100% of the elevator. Schindler claims the solar elevator saves energy, avoids power peaks when elevators start each journey and can operate independently of the power grid during power outages. The new solar elevator employs a regular Schindler 3,300 gearless machine room-less elevator, which is up to 60% more energy efficient than hydraulic elevators. Overall, this elevator system incorporates several energy-saving features, including a stable start, LED car lights, a frequency converter with an energy-efficient standby power mode, and control devices that automatically switch car lights to standby mode [36].

4.2 Circulating multi-car elevator system

In the case of conventional elevators, one car moves up and down the same elevator shaft. However, in a circulating multi-car elevator system, multiple cars (each equipped with a rotating magnetic array propulsion wheel) travel in the space of two conventional elevator shafts in a circulatory movement (**Figure 9**). This system is like a Ferris wheel, except instead of

having counterweights, each vehicle has its own motor. Hitachi was able to effectively verify this elevator system by using a replica that was only one-tenth of the actual size. Its prototype for circulating multi-care elevators uses the steel rope drive method. That is, in this system, two cars are connected to two steel circulating ropes making up one unit while the cars are placed in a diametrically opposite positions and driven by motors installed in the upper section of the building. The two cars are used as a mutual virtual counterweight and they achieve an energy saving of one-third compared to a system in which they are not counterweighted. Several sets of this circulating steel rope system with attached cars are combined and a motor controls the movement of each circulating rope set. Another feature of this elevator is the support rail system installed throughout the elevator shaft to guide the movement of the cars and prevent lateral sway motion. The revolving multi-car elevator is expected to not only enhance capacity but also decrease the required number of shafts and cut down on the amount of waiting time. Unfortunately, the current prototypes will need more safety improvement to meet international standards [37,38].

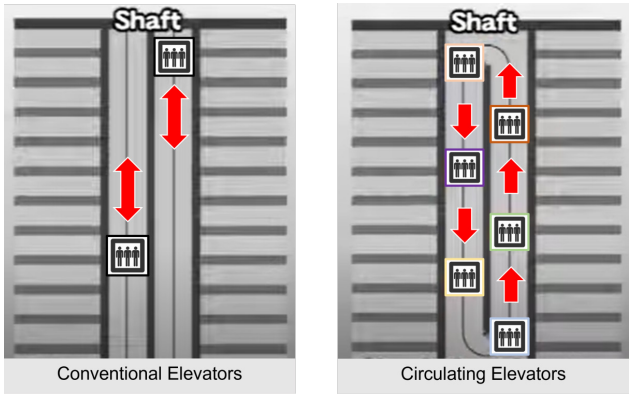

Figure 9. One car travels up and down the same elevator shaft in a traditional elevator system (left). In contrast, numerous cars in a circulating multi-car elevator system circulate between two conventional elevator shafts, each powered by a spinning magnetic array propulsion wheel (right).

Source: Adapted from youtube.com/watch?v=ESo-0KXeCFo.

4.3 Multi-directional elevators

Traditional elevators utilize cables to move a cabin strictly up and down. The MULTI, on the other hand, handles elevators more like a subway system. The cabins move sideways, frontways, and backways as well as up and down (**Figure 10**). Each system consists of numerous cabins individually powered by linear induction motors. Inspired by the TWIN concept, ThyssenKrupp created the first multi-car ropeless elevator system in 2017. Each car is propelled around a looping shaft by a motor system rather than ropes. As there are no ropes required to move the cars, this system is no longer height restricted. As such, MULTI offers a solution that allows increasing elevator height much above the KONE's 650-meter steel rope restriction. Because the MULTI uses many cars, it assures to reduce wait time. Finally, it promises to minimize energy use by integrating a "smart" device that reduces peak power demand by up to 60 percent, reducing the overall structure's carbon footprint [39,40].

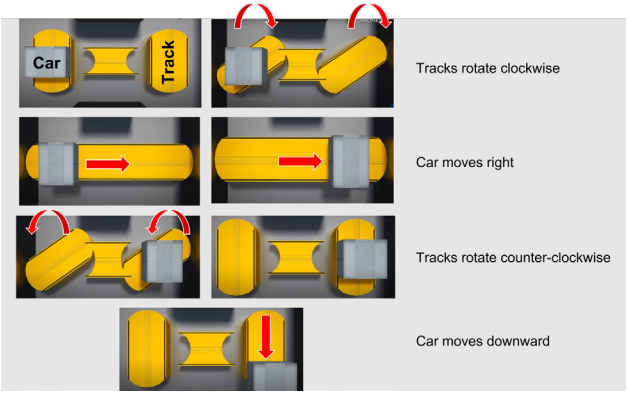

Figure 10. In a multi-directional elevator system, tracks rotate to allow cars change their directions.

Source: Adapted from youtube.com/watch?v=NBv1bkuj0Ac.

4.4 Robotization

Certainly, robotics technology will impact the construction of elevators and their shafts. Using robotics technology instead of humans will improve multiple prime areas, increase construction speed, reduce the energy used for construction and involved costs, enhance precision, and improve safety. Schindler has created a robot for the safe and exact installation of cabins using artificial intelligence and technology, paving the way for increased automation. This robot is fully autonomous and self-climbing,

and it moves through the elevator shaft to precisely measure and place the anchor bolts required for the installation of the elevator rails [39].

4.5 Drones

Similarly, drones are becoming more prevalent in the industrial and construction sectors and will have significant roles in constructing elevators. The installation of a new elevator entails numerous tedious, complicated, and costly activities, including the geometric measurements of wells to the certification checklists of field processes and inspection activities. Due to their mobility and ability to take photographs, drones can assist construction personnel. Drones might cut installation time by 21% to 26% and costs by 11% [40,41].

5. Conclusions

This article discusses the current technological advancements that help to make elevators "smarter". The concept of energy-generating elevators is gaining traction as a result of recent technological advancements [42]. The success of the communal environment in the vertical city depends on careful planning of the vertical transportation system. The planning team must have a thorough understanding of the varied demands that a mixed-use skyscraper will face due to its diverse purposes. Planning well can increase the transparency of logistical operations to the general public, renters, and inhabitants. The smoothest and least noticeable logistics operations are the best. If "smart" designs are used to integrate cutting-edge elevator technologies, they could lead to "greener" skyscrapers. Early cooperation among elevator manufacturers, builders, architects, urban designers, interior designers, and computer scientists may result in efficient solutions that further save costs, boost performance, and encourage efficiencies [43,44].

6. Future research

With the advent of COVID-19, elevator makers, engineers, and architects need to research ways to mitigate the possible spread of the coronavirus by elevators. Undoubtedly, applying social distancing within elevators is difficult because that reduces their effective capacity significantly. Alternatively, engineers may need to reconfigure the design of the elevators' air circulation system so that it prevents contamination and the spread of the virus [45,46].

Conflict of Interest

There is no conflict of interest.

References

[1] Fleischmann, C., Scherag, A., Adhikari, N.K., et al., 2016. Assessment of global incidence and mortality of hospital-treated sepsis. Current estimates and limitations. American Journal of Respiratory and Critical Care Medicine. 193(3), 259-272.

[2] Ahmed, A., Ge, T., Peng, J., et al., 2022. Assessment of the renewable energy generation towards net-zero energy buildings: A review. Energy and Buildings. 256, 111755.

[3] Oldfield, P., 2019. The sustainable impact of height. The Sustainable Tall Building. 3-25.

[4] Kim, S.H., 2017. Electric motor control: DC, AC, and BLDC motors. Elsevier: Amsterdam.

[5] Hamouche, W., Maurini, C., Vidoli, S., et al., 2017. Multi-parameter actuation of a neutrally stable shell: A flexible gear-less motor. Proceedings of the Royal Society A: Mathematical, Physical and Engineering Sciences. 473(2204), 20170364.

[6] Retolaza, I., Zulaika, I., Remirez, A., et al., 2021. New design for installation (DFI) methodology for large size and long life cycle products: Application to an elevator. Proceedings of the Design Society. 1, 2237-2246.

[7] Lin, K.Y., Lian, K.Y. (editors), 2017. Actual measurement on regenerative elevator drive and energy saving benefits. 2017 International Automatic Control Conference (CACS); 2017 Nov 12-15; Pingtung, Taiwan. USA: IEEE. p. 1-5.

[8] Erica, D., Godec, D., Kutija, M., et al. (editors),

2021. Analysis of regenerative cycles and energy efficiency of regenerative elevators. 2021 International Conference on Electrical Drives & Power Electronics (EDPE); 2021 Sep 22-24; Dubrovnik, Croatia. USA: IEEE. p. 212-219.

[9] Kutija, M., Pravica, L., Godec, D. (editors), et al., 2021. Regenerative energy potential of roped elevator systems-a case study. 2021 IEEE 19th International Power Electronics and Motion Control Conference (PEMC); 2021 Apr 25-29; Gliwice, Poland. USA: IEEE. p. 284-291.

[10] Al-Kodmany, K., 2015. Tall buildings and elevators: A review of recent technological advances. Buildings. 5(3), 1070-1104.

[11] Yang, D.H., Kim, K.Y., Kwak, M.K., et al., 2017. Dynamic modeling and experiments on the coupled vibrations of building and elevator ropes. Journal of Sound and Vibration. 390, 164-191.

[12] Yaman, O., Karakose, M. (editors), 2017. Auto correlation based elevator rope monitoring and fault detection approach with image processing. 2017 International Artificial Intelligence and Data Processing Symposium (IDAP); 2017 Sep 16-17; Malatya, Turkey. USA: IEEE. p. 1-5.

[13] Mohaney, S., Shah, M., 2015. Emerging trends in vertical elevating system. International Journal of Engineering and Management Research (IJEMR). 5(1), 51-56.

[14] Hirasawa, K., Eguchi, T., Zhou, J., et al., 2008. A double-deck elevator group supervisory control system using genetic network programming. IEEE Transactions on Systems, Man, and Cybernetics, Part C (Applications and Reviews). 38(4), 535-550.

[15] Cortes, P., Munuzuri, J., Vazquez-Ledesma, A., et al., 2021. Double deck elevator group control systems using evolutionary algorithms: Interfloor and lunchpeak traffic analysis. Computers & Industrial Engineering. 155, 107190.

[16] Li, K., Mannan, M.A., Xu, M., et al., 2001. Electro-hydraulic proportional control of twin-cylinder hydraulic elevators. Control Engineering Practice. 9(4), 367-373.

[17] Gichane, M.M., Byiringiro, J.B., Chesang, A.K., et al., 2020. Digital triplet approach for real-time monitoring and control of an elevator security system. Designs. 4(2), 9.

[18] Siikonen, M.L., 2021. People flow in buildings. John Wiley & Sons: New York.

[19] Makar, M., Pravica, L., Kutija, M., 2022. Supercapacitor-based energy storage in elevators to improve energy efficiency of buildings. Applied Sciences. 12(14), 7184.

[20] Ma, X., Chengkai, L., Ng, K.H., et al., 2020. An Internet of Things-based lift predictive maintenance system. IEEE Potentials. 40(1), 17-23.

[21] Parker, D., Wood, A., 2013. One world trade center, New York, USA. The tall buildings reference book. Routledge: London. p. 496-501.

[22] Lewis, K., Holt, N., 2011. Case study: One world trade center, New York. CTBUCH Journal. 3.

[23] Gershon, R.R., Qureshi, K.A., Rubin, M.S., et al., 2007. Factors associated with high-rise evacuation: qualitative results from the World Trade Center Evacuation Study. Prehospital and Disaster Medicine. 22(3), 165-173.

[24] McAllister, T.P., Sadek, F., Gross, J.L., et al., 2013. Overview of the structural design of World Trade Center 1, 2, and 7 buildings. Fire Technology. 49, 587-613.

[25] Langewiesche, W., 2010. American ground: Unbuilding the world trade center. North Point Press: San Francisco.

[26] Xia, J., Poon, D., Mass, D., 2010. Case study: Shanghai Tower. CTBUH Journal. 11, 12-18.

[27] Zhaoa, X., Ding, J.M., Suna, H.H., 2011. Structural design of shanghai tower for wind loads. Procedia Engineering. 14, 1759-1767.

[28] Jiang, H.J., Lu, X.L., Liu, X.J., et al., 2014. Performance-based seismic design principles and structural analysis of Shanghai Tower. Advances in Structural Engineering. 17(4), 513-527.

[29] Zhang, Q., Yang, B., Liu, T., et al., 2015. Structural health monitoring of Shanghai Tower considering time-dependent effects. International Journal of High-rise Buildings. 4(1), 39-44.

[30] Gensler, A.M., Winey, D., Xia, J., et al., 2015. Shanghai Tower. Oro Editions: San Francisco.

[31] Goldsworthy, K., 2018. Burj Khalifa. Weigl Publishers: New York.

[32] Abdelrazaq, A. (editor), 2010. Design and construction planning of the Burj Khalifa, Dubai, UAE. Structures Congress 2010; 2010 May 12-15; Orlando, Florida, United States. USA: American Society of Civil Engineers. p. 2993-3005.

[33] Ponzini, D., Alawadi, K., 2022. Transnational mobilities of the tallest building: origins, mobilization and urban effects of Dubai's Burj Khalifa. European Planning Studies. 30(1), 141-159.

[34] Feblowitz, J.C., 2010. Confusing the wind: The Burj Khalifa, mother nature, and the modern skyscraper. Inquiries Journal. 2(01).

[35] Soni, K.M., Bhagat Singh, P., 2020. First onsite net zero energy green building of India. International Journal of Environmental Science and Technology. 17(4), 2197-2204.

[36] Dotson, D.L., Eddy, J., Swan, P., 2022. Climate action and growing electricity demand: Meeting both challenges in the 21st century with space-based solar power delivered by space elevator. Acta Astronautica. 198, 761-766.

[37] Bohn, G., Steinmetz, G., 1984. The electromagnetic levitation and guidance technology of the transrapid test facility Emsland. IEEE Transactions on Magnetics. 20(5), 1666-1671.

[38] Gerstenmeyer, S., 2018. Traffic analysis for a multi car lift system used as local group. 9th Symposium on Lift and Escalator Technologies. 9(1), 253-262.

[39] Babel, F., Hock, P., Kraus, J., et al. (editors), 2022. Human-robot conflict resolution at an elevator-the effect of robot type, request politeness and modality. 2022 17th ACM/IEEE International Conference on Human-Robot Interaction (HRI); 2022 Mar 7-10; Hokkaido, Japan. USA: IEEE. p. 693-697.

[40] Marani, Y., Telegenov, K., Feron, E., et al. (editors), 2022. Drone reference tracking in a non-inertial frame using sliding mode control based Kalman filter with unknown input. 2022 IEEE Conference on Control Technology and Applications (CCTA); 2022 Aug 23-25; Trieste, Italy. USA: IEEE. p. 9-16.

[41] Kougawa, Y., Omachi, A., Iwase, S., et al., 2017. Hitachi's core concept for elevator and escalator products and services, and concept model. Hitachi Review. 66(3), 197.

[42] Yanbin, Z., Shuangchang, F., Zheyi, L., et al. (editors), 2020. Research on intelligent lighting system of elevator ground gap. 2020 International Conference on Intelligent Computing and Human-Computer Interaction (ICHCI); 2020 Dec 4-6; Sanya, China. USA: IEEE. p. 25-28.

[43] Dbouk, T., Drikakis, D., 2021. On airborne virus transmission in elevators and confined spaces. Physics of Fluids. 33(1), 011905.

[44] Harris, T.M., Eranki, P.L., Landis, A.E., 2019. Life cycle assessment of proposed space elevator designs. Acta Astronautica. 161, 465-474.

[45] Kong, T., Hu, T., Zhou, T., et al., 2021. Data construction method for the applications of workshop digital twin system. Journal of Manufacturing Systems. 58, 323-328.

[46] Nouri, Z., Norouzi, N., Ataei, E., et al., 2021. Virologic microparticle fluid mechanics simulation: COVID-19 transmission inside an elevator space. International Journal of Computational Materials Science and Engineering. 10(02), 2150007.

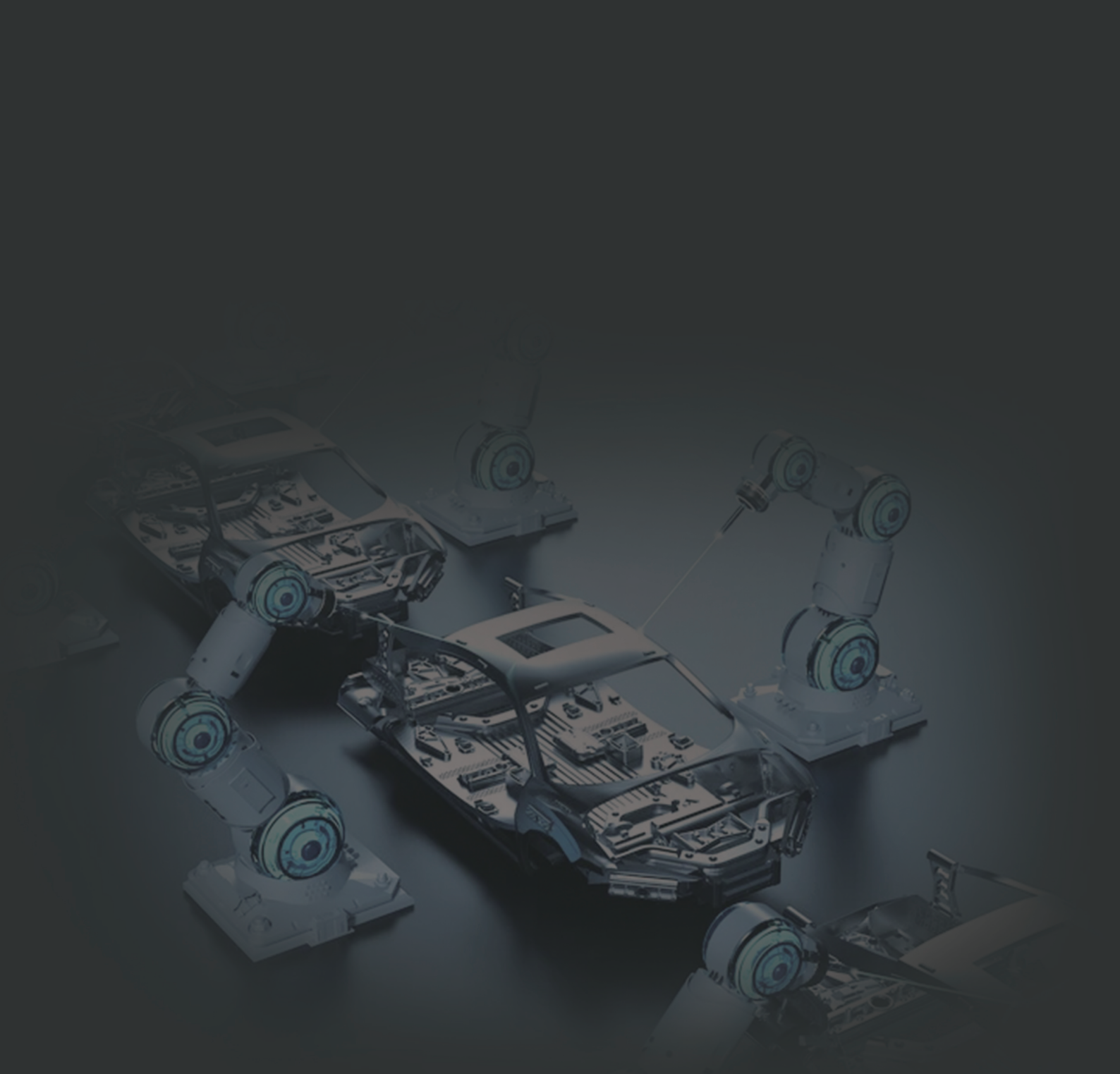

BILINGUAL
PUBLISHING GROUP
Pioneer of Global Academics Since 1984

Tel:+65 65881289
E-mail: contact@bilpublishing.com
Website:https://journals.bilpubgroup.com

2810-935X
01
9 772810 935230